Politecnico di Torino

Master thesis
2D ferromagnets for spintronics

Master degree in Nanotechnologies for ICTs

Laboratory supervisors:
Frédéric Bonell
Matthieu Jamet
Academic supervisors:
Carlo Ricciardi
Paolo Allia

Authors: s265808 Giulio Gentile

October 12, 2020

List of Figures

Abstract

After the discovery of graphene, the field of 2D materials has awaken an impressive amount of interest in the scientific community.

These materials stable in 2D, are layered materials, where each layer stacks on the others interacting by van der Waals (vdW) interactions.
Due to the weak nature of this interaction, they can be grown epitaxially in presence of large mismatch and it is possible to combine them in heterostructures.

The family includes a wide range of properties, including metals, insulators, topological insulators, semiconductors, superconductors. The class of 2D ferromagnetic materials has been intensively investigated only recently, as most articles have been published just in the last years, from 2017.
Among these, the vast majority are based on mechanical exfoliation, obtaining μm-size flakes. Our goal is to develop the epitaxy of van der Waals materials and heterostructures on cm2 areas.

The field of spintronics regards the information processing based on the electron spin instead of its charge. 2D materials have been identified as high potential materials for spintronics and are currently being investigated.

In this work, done in the "2D and semiconductor spintronics" team of Spintec (Univ. Grenoble Alpes/CEA/CNRS), we investigate the epitaxial growth of ferromagnet Fe_3GeTe_2 by molecular beam epitaxy (MBE), which is a fundamental step to pave the way for studies of heterostructures and devices, also combining other 2D van Der Waals materials with exotic properties, for instance topological insulators. In the following chapters scientific background and motivations will be discussed first, second the experimental techniques used will be elaborated, in the third experimental results will be detailed, and conclusions in the last chapter.

CHAPTER 1

Scientific background and motivations

1.1 2D materials

Following the exfoliation of graphene in 2004 [1], a large interest has been awaken for the study of two-dimensional (2D) materials.
These are stable crystalline materials consisting of a single layer of atoms, a monolayer (ML), e.g. graphene ML is one carbon atom thick with an honeycomb lattice. An important family of 2D materials is composed by transition metal dichalcogenides (TMDs) [2], whose formula unit is MX_2, where M is a transition metal, X a chalcogenide, showing a variety of exotic properties. TMDs have hexagonal structure, with monolayers composed by three sublayers (X-M-X).
2D materials can have dramatically different properties than their bulk counterparts, also due to the dominating effects of the surface, and the strong confinement of carriers in the case of conductors.
These materials have strong, covalent intralayer bonds but weak van Der Waals interactions between different layers, for this reason it is possible to combine them, forming van Der Waals (vdW) heterostructures with well defined sharp interfaces. These structures do not simply lead to the addition of functionalities, but interactions across interfaces can give rise to proximity effects: properties of 2D layers are altered by those of neighbouring layers. Other exotic effects can occur, for instance Kosterlitz-Thouless phase transition, in some materials many-body effects as superconductivity, charge density waves and spin density waves.
Stable 2D materials found can have wide range of properties, including metals as $VSe2$ [3], $PtSe2$ [4], insulators as hexagonal boron nitride [5], topological insulators as Bi_2Se_3, WTe_2 [6], semiconductors as WSe_2 [7], $MoSe_2$ [8], superconductors as $NbSe_2$ [9].

Spintronics based only on 2D materials is an appealing perspective and it requires the development of 2D magnetic materials, which will be introduced in the following section.

1.2 2D magnetic crystals

The class of 2D ferromagnets has been emerging only in the last few years, from 2017. When considering the first predictions on 2D magnetism, the Mermin-Wagner-Hohenberg theorem demonstrates that for a finite, short range interaction in 2D systems, thermal fluctuations can destroy long range magnetic order at finite temperature.[10] While this is true for an ideal isotropic Heisenberg model, the results of the theorem do not strictly hold in presence of anisotropy, and magnetic order can exist. In most cases, the Curie temperature of the 3D is higher than the 2D counterpart. If layered material is ferromagnetic in 3D, the existence of such order in 2D individual monolayers is not granted, and depends on the anisotropy of the system. For instance, when reducing the number of $Cr_2Ge_2Te_6$ layers the critical temperature goes to zero when reaching the monolayer limit. [11] In other cases, spin–orbit coupling causing anisotropy, can help magnetism exist even in the monolayer limit, as for CrI_3 [12].

The first observation of long range order in pristine 2D materials regarded $Cr_2Ge_2Te_6$ [11] and CrI_3 [13], in 2017. Both are insulators. $Cr_2Ge_2Te_6$ is a 2D Heisenberg ferromagnet with small anisotropy, Its reported Curie temperature is $T_c = 68K$ in bulk form, $T_c = 30K$ in bilayer form.
CrI_3 is antiferromagnetic for an even number of layers, ferromagnetic for an odd number of layers (fig: 1.2), with order surviving down to the monolayer limit. CrI_3 has a Curie temperature of $T_c = 61K$ in bulk form and $T_c = 45K$ for a single monolayer.

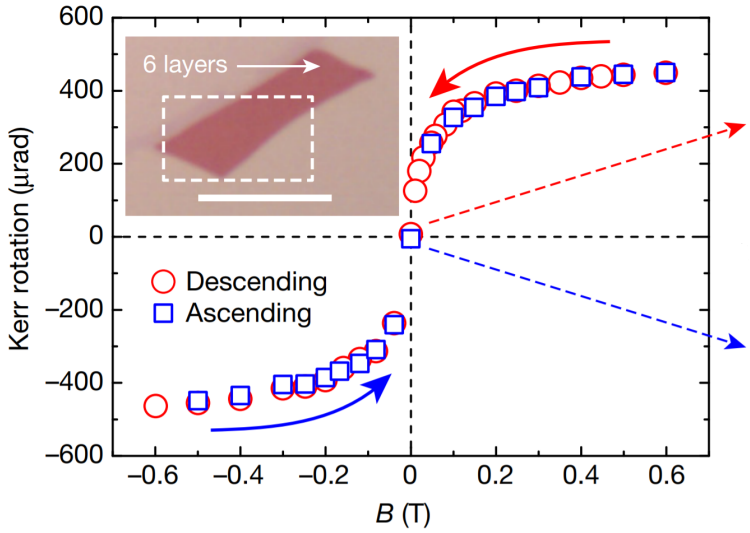

Figure 1.1: MOKE measurements for few-layer $CrGeTe_3$. Blue and red correspond to forward and backward field scanning directions. The inset shows an optical image of the sample, scale bar is $10\mu m$, from [11]

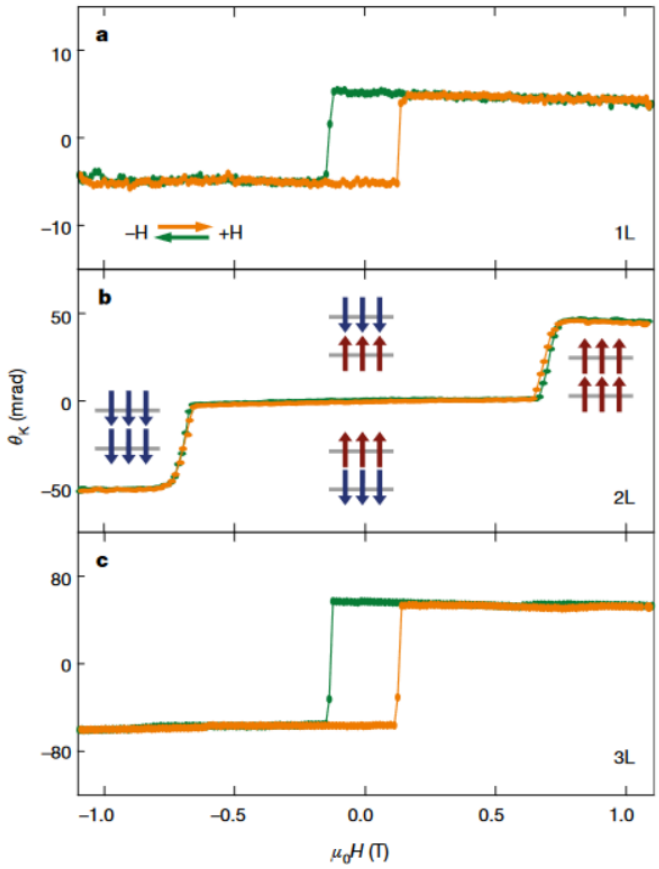

Figure 1.2: MOKE measurements demonstrating layer-dependent magnetism in atomically-thin CrI3. a) monolayer (1L) CrI3, showing hysteresis in the Kerr rotation as a function of applied magnetic field, indicative of ferromagnetic behaviour. b), CrI3 bilayer showing vanishing Kerr rotation for applied fields ± 0.65 T, indicating antiferromagnetism. Insets bilayer (2L) magnetic ground states for different applied fields. c), trilayer (3L) flake, showing again ferromagnetic behaviour, from [13]

Fe_3GeTe_2 is an 2D itinerant ferromagnet, with a $T_c = 216.4K$ for bulk samples [14], $T_c \approx 130K$ for a single monolayer and sizable perpendicular anisotropy. First first fabricated in 2006 [15] and 2D ferromagnetism reported first in 2018 it is a vdW layered material, composed of monolayers $\approx 8.2\mathring{A}$ thick with an hexagonal structure.

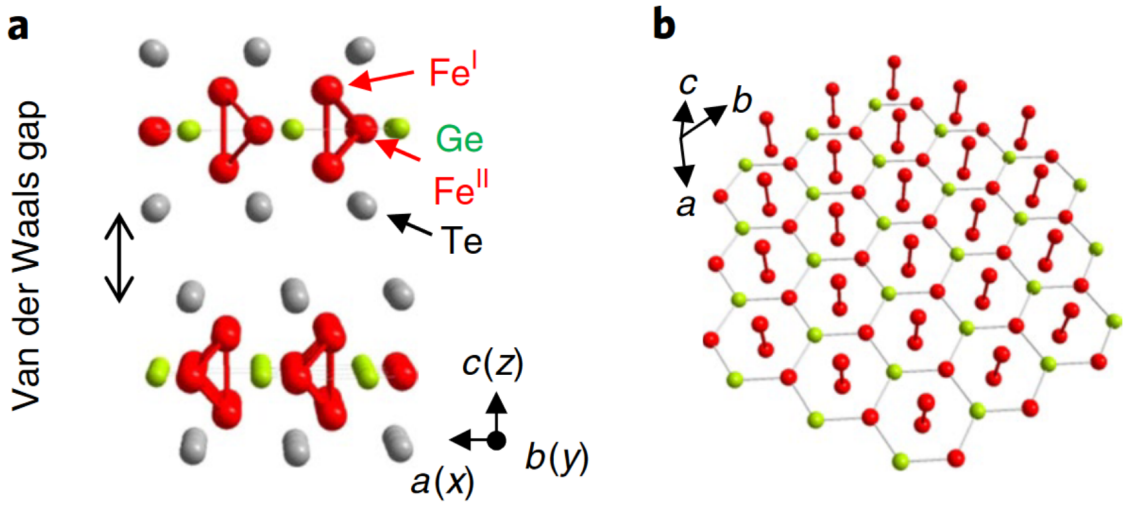

Figure 1.3: a) Structure of Fe_3GeTe_2 bilayer. b) Structure of a Fe_3Ge monolayer, from [16]

Each layer is formed by five sublayers: (fig: 1.3)

- Te layer
- a sublayer of Fe Ge atoms honeycomb lattice
- Fe-Fe dumbbells placed at the centre of each hexagon of the honeycomb
- Te layer

Some experimental studies on this material have been published: molecular beam epitaxy of FGT [14], anomalous Hall effect in FGT [16], early studies of gating, leading to room temperature ferromagnetism [17], spin orbit torques at FGT/Pt interface [18]. composition tuning [14] [19].

1.3 Project motivations

The field of spintronics regards the information processing based on the electron spin instead of its charge. FGT is a good candidate, since has perpendicular anisotropy and compared to CrI_3 and $Cr_2Ge_2Te_6$ has higher Curie temperature and is a conductor. As 2D ferromagnetic layer in all vdW heterostructures, where each layer could be grown epitaxially with molecular beam epitaxy (MBE).

For instance, study of spin orbit torques in heterostructures formed by topological insulator on 2D FM, or TMD on 2D FM .
Spin orbit torque uses a spin current polarized by a material with large spin orbit coupling. injecting a charge current flowing in plane (i.e. x direction), we also obtain a spin current in the normal direction (i.e z direction), that will exert a torque on the adjacent magnetic layer. Large torque requires:

- Large charge-spin conversion
- Very thin FM (interfacial effect)
- no shunting by FM
- Clean interface

Good stability for data retention requires a large FM anisotropy per volume product. For these reasons, all-vdW stacking of TI or TMD /2D FM can be a good candidate. The Spintec laboratory is focused on development of spintronic devices, allowing to process information based on magnetism and electrons spin degree of freedom. Main spintronic 2D materials are appealing, but more work has to be done to achieve efficient electrical control of 2D magnets, long distance transport of spins efficient tunneling and injection of spins in spintronic devices.
In particular 2D magnets can provide non-volatile storage and enable spin filtering, injection and detection [20].

To obtain these structures and observe the related physical phenomena it is important to epitaxially grow crystals. A variety of techniques could be used to obtain van Der Waals epitaxy, such as CVD, pulsed laser deposition, and molecular beam epitaxy (MBE).

Currently, most publications regarding van Der Waals materials are based on exfoliation and transfer of films, which is not a reproducible process and gives very small area films, which can be harder to study.

MBE has many advantages:

- Growth occurs in a ultra high vacuum environment (UHV) ($< 10^{10} Torr$)
- Slow growth rates ($\sim nm/min$), necessary to grow heterostructures with abrupt interfaces.
- Source materials are ultra pure (typical purity of 99.999% (5N) or 99.9999% (6N)).
- Growth of large, cm scale films.
- Growth of van Der Waals heterostructure.
- In situ characterization tools, e.g. RHEED, XPS, AFM..).

For these reasons, MBE can be considered an optimal technique to study novel devices with well defined staggered interfaces.

CHAPTER 2

Experimental techniques

2.1 Molecular Beam Epitaxy (MBE)

MBE is an epitaxial growth technique allowing growth of nanomaterials. The deposition occurs by evaporation/sublimation of ultra-pure materials in a ultra high vacuum (UHV) chamber.
The molecular beams evaporated/sublimated, with typical vapour pressure of $10^{-4} mbar$ posses mean free paths larger than growth chamber size, do not interact in the gas phase and are highly directional.

Combining good control of molecular beams with the use of mechanical shutters to control the deposition, several materials can be independently evaporated, with a typical growth rate of 1-10 atomic layers per minute, allowing submonolayer control of the growth, doping and possibility to grow heterostructures with sharp interfaces. A typical configuration of an MBE machine is represented in fig: 2.1, where the main components are represented. In the following sections we detail the different components of the MBE system present at Spintec.

2.1.1 Vacuum

Every time the chamber is opened, the chamber must be baked at $150 - 200°C$, i.e. in order to achieve very low background pressure it is necessary to desorb molecules from surfaces inside the machines. It is a slow process, as the chamber is externally heated for several days (typically 1-2 weeks), while pumping with the turbopump.

Very low pressures $\approx 10^{-10}$ *torr* are fundamental to: reduce impurity concentration in growth chamber, increase the mean free path of both evaporated material and electrons and allow the use of in situ electron diffraction techniques (RHEED).

The chamber is brought to ultra high vacuum by a series of pumping systems:

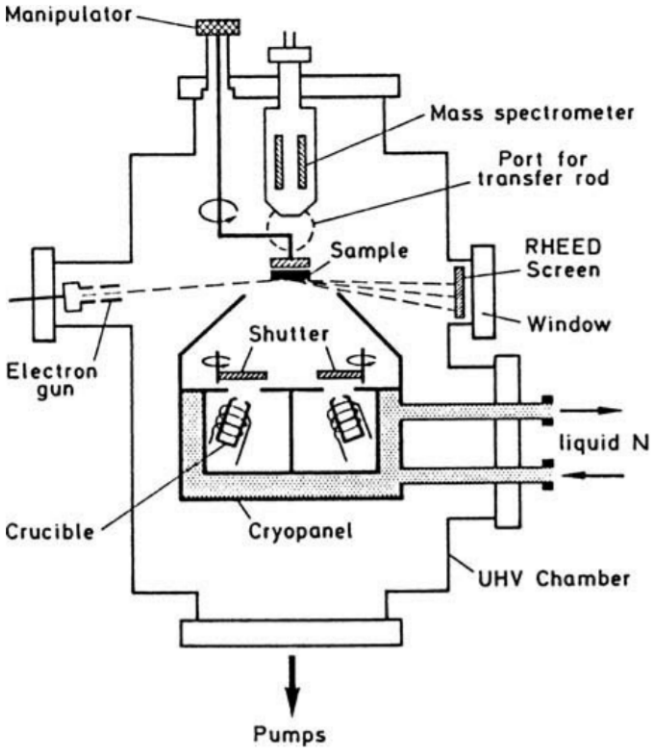

Figure 2.1: Schematic of a typical MBE machine, from [21]

deposition chamber is pumped by a large turbo-molecular pump. When the pressure is lower than about $10^{-5}mbar$, the chamber is directly pumped with a cryopump and the turbomolecular pump is stopped. Before before each growth cryopanels are filled with liquid nitrogen, furthermore reducing pressure by cryopump effect.

Samples and substrates can only be brought outside by means of a load chamber and a load-lock; in such a way the main chamber is always kept in vacuum, reducing load time and reducing impurity concentration. Load-lock can be brought at atmospheric pressure by filling it with nitrogen, as air would lead to a detrimental humidity absorption on load chamber surfaces.
The pressure is measured with an ionization gauge, where gas particles are ionized, accelerated and collected, giving rise to a measurable current.

2.1.2 Material evaporation

Material evaporation consists in heating the material to a temperature where sizable evaporation/sublimation occurs (around $10^{-4}mbar$ vapor pressure at the material surface, yielding $10^{-7}mbar$ at the sample surface and 1-10ML growth rate).

Two common evaporation sources are effusion cells (also called Knudsen cells) and electron beam evaporators.

In an effusion cell, the material is placed in a tube crucible surrounded by a fila-

ment heated by Joule effect. The temperature is precisely tuned using a PID controller, which sets the current of the heating coil, and a thermocouple as feedback. Achieving a good control of this parameter is fundamental, as the partial pressure of the beam depends exponentially on the cell temperature. Some elements like Se, Te or As are known to evaporate as clusters of several atoms. These clusters are less reactive than individual atoms, so that high evaporation rates are required. Cracker cells circumvent this problem. A temperature gradient is applied along the crucible. The low temperature zone contains the material, while the zone close to the aperture is heated to a much higher temperature to crack the evaporated clusters. In our case, Ge was evaporated from a standard cell heated around 1000°C. Te was evaporated from a cracker cell with three zones heated around 300°C, 500°C and 1000°C, respectively.

Electron beam evaporation was used to sublimate Fe. In this case, the material is bombarded by high energy (keV) electrons. We set the electron gun filament current and high voltage to extract and accelerate the electrons, which are then deflected by a magnetic field onto the liner. Then, using a quartz microbalance crystal monitor exposed to the beam, we can measure the evaporation rate in real time and control the e-gun parameters with a feedback loop. E-beam evaporation allows to reach higher temperatures than effusion cells and is typically used for refractory elements. On the other hand, stable very low evaporation fluxes are more difficult to achieve.

2.1.3 Manipulator

The manipulator in the growth chamber allows to rotate and place the sample in growth position, transfer position and allows to place a ionization gauge in front of the molecular beam to measure its partial pressure.

Manipulator also allows to control the substrate temperature by means of a heating coil, thermocouple and a PID controller. The substrate temperature is another fundamental parameter, as during growth it influences the surface mobility of adatoms, sticking coefficients, absorption/desorption rates, activation of surface reactions.
It is also important to note that, even if the manipulator thermocouple can be calibrated, the value of substrate temperature we set and measure may be far from the actual one, due to the non ideal thermal coupling of substrate and manipulator in UHV.
In our case, the temperature was calibrated by tracking with RHEED the solid/liquid transition of well-known eutectic alloys, estimating a $\Delta T \approx 40°C$ between the measure and the actual values. This calibration was made with alloys attached to the sample holder with indium, so with a very good thermal contact.
In the case of substrates used for growth, they are just pressed against the sample holder, so the actual T_{sub} is most probably lower than the reading.

2.2 Reflection high energy electron diffraction (RHEED)

RHEED is an electron diffraction technique used for structural analysis of surfaces.
It provides semi-quantitative information on the surface structure, giving real time in situ characterization, regarding the degree of crystallinity of the surface.
In the case of layer-by-layer growth also allows to monitor in real time the formation of each monolayer (RHEED intensity oscillations).
An electron beam is accelerated by a high voltage ($12keV$ in our case) towards the sample, impinging at a low grazing angle, as in fig: 2.2.
At this energy, the electron mean free path is of the order of 100nm.

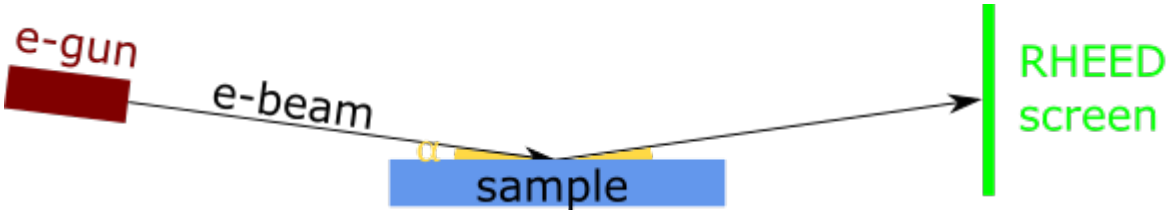

Figure 2.2: RHEED setup

However, the low angle of incidence ($\sim 1°$) ensures a penetration depth of less than 0.1 nm in the direction perpendicular to the surface.
RHEED is therefore sensitive to the first atomic plane.
Electrons scattered from atoms within a small region, characterized by the electron coherence length, can interfere, giving rise to diffraction patterns on a fluorescence screen.
In our system this screen is placed $\approx 25cm$ away from the sample, emitting light when excited by electrons of high enough energy.
RHEED diffraction experiments allow to gain information on the 2D reciprocal lattice of the surface, which in turn can give information of the surface structure (direct lattice).
Waves reflected by different lattice planes normal to the surface can interfere constructively, if they satisfy Bragg's law.
From the reciprocal lattice point of view, Von Laue condition for 2D crystals must be satisfied:

$$\mathbf{k}'_{\parallel} - \mathbf{k}_{\parallel} = \mathbf{G}_{\parallel}$$

where

$$\mathbf{G}_{\parallel} = h\ \mathbf{a}_1^* + k\ \mathbf{a}_2^*$$

is a reciprocal lattice vector, h,k integers, $\mathbf{k}_{\parallel}$ and $\mathbf{k}'_{\parallel}$ are incident and reflected wavevectors.
This condition is similar to the Von Laue condition for 3D crystals; but concerns only projections of the wavevectors on the surface, i.e. we have a relaxation of the third

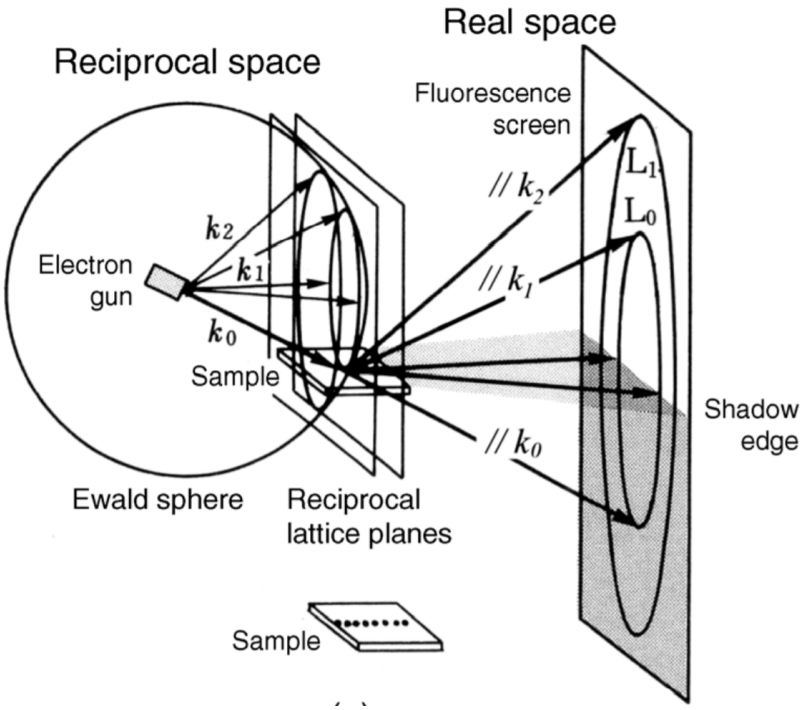

Figure 2.3: Depiction of diffraction in a RHEED experiment, from [22]

Von Laue condition, which regards the direction z normal to the surface.
It is possible to describe the interference condition in reciprocal space by defining the Ewald sphere, as in fig. 2.3. The constructive interference condition is satisfied for wavevectors $\mathbf{k}'_{\parallel}$ given by the intersections of the 2D reciprocal lattice (set of lines parallel to z) with the Ewald sphere, having radius k.
In practice, given the large kinetic energy of electrons, the radius of the Ewald sphere is much larger than the spacing between reciprocal lattice rods, so we can locally approximate the surface as a plane. The intersection of a sphere with lines gives points, however, in reality there is some dispersion on the incident wavevector $\mathbf{k}$:

$$\mathbf{k} = \mathbf{k}_0 + \Delta\mathbf{k}$$

in other words, the Ewald sphere as a finite thickness Δk.
In addition, because of crystal imperfections, the lines of the 2D reciprocal lattice are actually cylinders with a finite radius. Therefore, the actual intersection of the Ewald sphere with the reciprocal lattice gives rods with finite length and width (fig: 2.4 b).

Considering a well ordered monocrystalline surface, the RHEED pattern will show well defined and contrasted vertical rods, whose spacing corresponds to the reciprocal lattice distance obtained considering the lattice distances in the direction parallel to the screen.
If the surface is not monocrystalline, RHEED pattern will be affected, as described by fig: 2.4. The presence of defects will broaden these rods, reducing the contrast, In

presence of 3D features, electrons partially penetrating will introduce brighter spots and modulation along the rods (fig:2.4 d,f), reminiscent of bulk diffraction (transmission electron diffraction). Domains or steps can possibly induce a splitting of the streaks, if they occur in a periodic way. (fig:2.4 c,e)

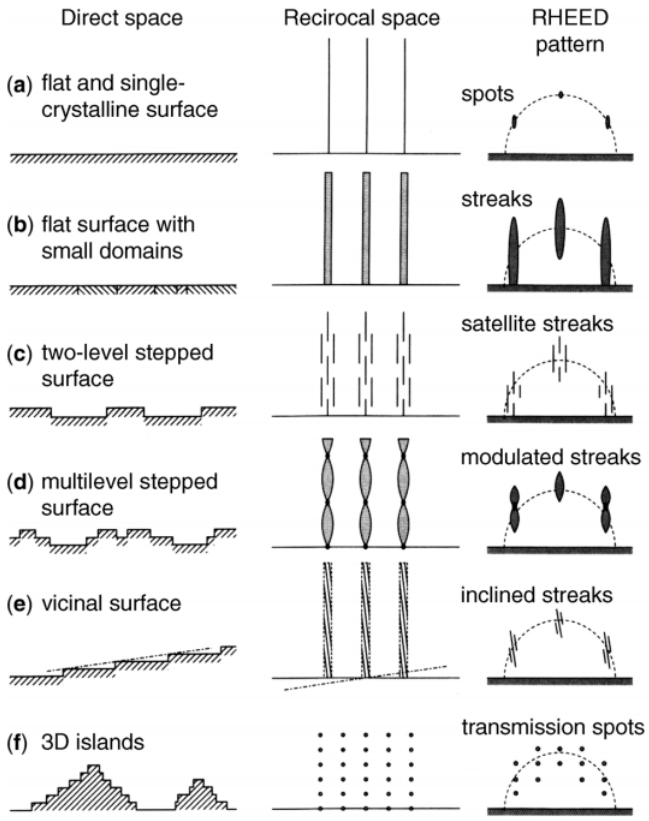

Figure 2.4: Interpretation of different RHEED patterns, from [22]

Coherence of the electron beam

An ideal source can be described by a single plane wave $Ae^{i\mathbf{k}\cdot\mathbf{r}}$ with an infinite coherence length. In this case, the electrons scattered by all the exposed atoms would interfere with each other. However, in practice electron sources are not perfectly monochromatic and have a finite divergence $\Delta\theta$, which reduce their coherence length to $\sim 5nm$. Therefore, scattered waves within few nm produce interferences, as if irradiated by an ideal plane wave, whereas waves scattered by more distant objects add in intensity.
No structure on a scale larger than the coherence length can give rise to a diffraction pattern.
We can define the transverse coherence length l_T [22]:

$$l_T = \frac{\lambda}{\sqrt{2}\ \Delta\theta} \tag{2.1}$$

where λ is the electron wavelength, $\Delta\theta$ is the divergence angle of the beam.

2.2.1 Diffraction from a 2D crystal

Considering the surface structure of the hexagonal lattice, we can define the 2D surface lattice vectors in real space $\mathbf{a}_1$ $\mathbf{a}_2$, and then the corresponding reciprocal lattice vectors in k-space $\mathbf{a}_1^*$ $\mathbf{a}_2^*$, as in fig: 2.5.

$$\mathbf{a}_1^* = 2\pi \frac{\mathbf{a}_2 \times \hat{\mathbf{n}}}{|\mathbf{a}_1 \times \mathbf{a}_2|}, \quad \mathbf{a}_2^* = 2\pi \frac{\hat{\mathbf{n}} \times \mathbf{a}_1}{|\mathbf{a}_1 \times \mathbf{a}_2|}$$

where $\hat{\mathbf{n}}$ is the unit vector normal to the surface.
The following hold:

$$\mathbf{a}_i^* \cdot \mathbf{a}_j = 2\pi\delta_{ij} \text{ and } |\mathbf{a}_i^*| = 2\pi \left[\mathbf{a}_i \sin(a_i a_j)\right]^{-1}, \quad i,j = 1,2 \tag{2.2}$$

Reciprocal lattice vectors are defined as follows:

$$\mathbf{G}_{\parallel} = h\mathbf{a}_1^* + k\mathbf{a}_2^*$$

where integer numbers h, k are the Miller indices.

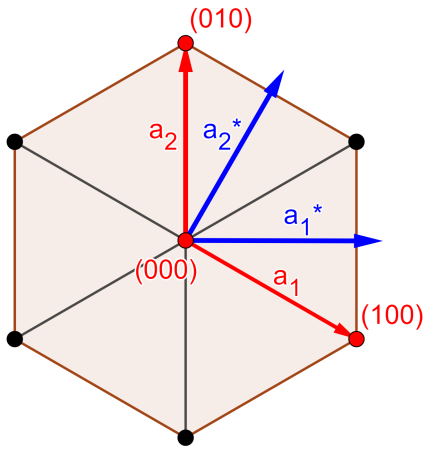

Figure 2.5: Hexagonal lattice. The unit cell is the polygon enclosed between the points (000), (100), (110) and (010), defined by the lattice vectors a_1 a_2. The corresponding reciprocal lattice vectors a_1^* a_2^* are also represented.

If we consider the full reciprocal lattice, higher diffraction order arise, as the Ewald sphere can intersect with reciprocal rods, corresponding to higher order reciprocal lattice points. Fig: 2.6 shows a larger portion of the reciprocal space, along with Ewald spheres related to two possible electron beam incident directions, with k-vectors $\mathbf{k}_1$, $\mathbf{k}_2$.
Changing the direction of the beam, the Ewald sphere will intersect different reciprocal lattice rods, thus giving rise to distinct diffraction patterns as a function of the

azimuthal angle.

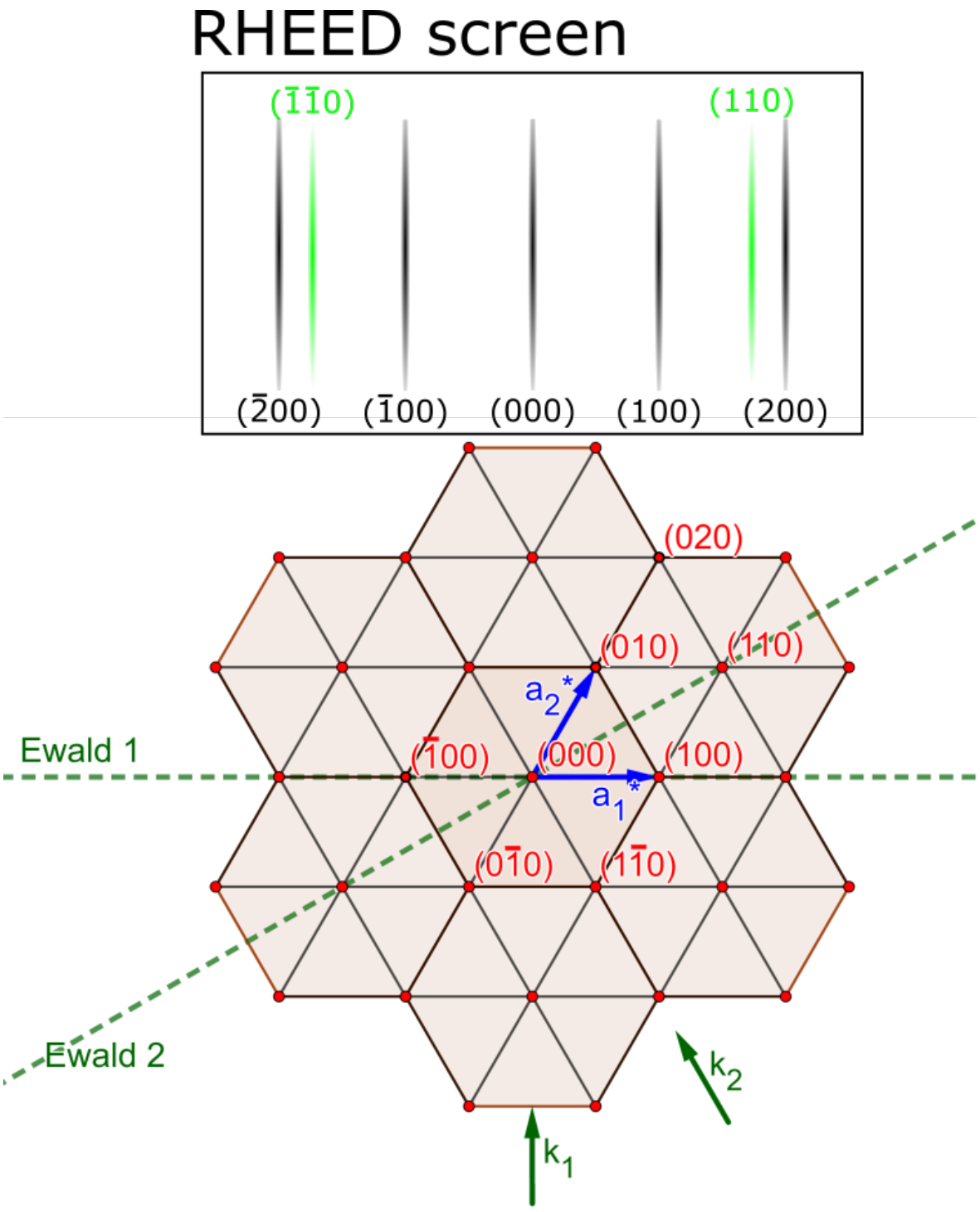

Figure 2.6: Impinging with a k-vector k_1, intercepts of Ewals sphere with lattice points determines the position of rods in the RHEED pattern.(black) Considering k_2 direction instead, other rods appear (depicted in green on the screen).

2.3 X-ray photoelectron spectroscopy (XPS)

X-ray photoelectron spectroscopy (XPS) is a surface chemical characterization technique based on photoelectric effect.
In XPS, photons of known energy $h\nu$ are used to excite core level electrons of the sample, which can acquire enough energy to escape the surface.
It must be noticed that while photons can penetrate deeper $\sim 0.1 - 1\mu m$ into the sample, the emitted electrons are coming from a much thinner portion ($< 10nm$), as electron escape length is shorter.
The emitted electrons are collected, and their energy spectrum can be analysed to obtain binding energies of core level electrons, and thus the chemical signature of the surface. The measured spectrum is composed of a set of characteristic peaks, superimposed on a background signal due to secondary electrons, i.e. electrons that due to multiple scattering have lost energy while propagating in the crystal.
The sharp peaks in the spectrum correspond a kinetic energy: $E_K = h\nu - E_B - \Phi$ where $h\nu$ is photon energy, Φ is the workfunction, E_B is the binding energy of the initial state, which embeds the chemical information we want to obtain.
To avoid scattering of particles, the experiment is carried in UHV.
In our case the XPS system is not connected to the growth chamber, therefore, we need to transfer the samples in air before measurements. We used an equipment composed of a dual-anode X-ray source (Al K_α: 1487eV and Mg K_α: 1253eV) operated at 300W, a cylindrical mirror analyser and a channeltron (electron multiplier).

2.4 in plane X-Ray diffraction (XRD)

XRD is a widely used structural characterization technique.
In grazing incidence configuration the scattering vector lies in plane as diffraction is due to planes normal to the surface. The XRD diffraction experiments, in the particular configuration we used, can be compared to RHEED, but there are some notable differences:

- photons interact less with matter, so measurements are done in air
- photons have larger penetration than electrons. Even in grazing geometry, we see the full film and the substrate
- As photons interact less with matter and the geometry is more controlled; intensity is easier to understand, can be analysed quantitatively.

With XPS is possible to estimate the average lattice parameter and mosaicity (misorientation of grains).

2.5 Magnetic measurements

To gain information on the magnetic properties of the grown film two techniques were employed:
Magneto optical Kerr effect (**MOKE**)
Anomalous Hall effect (**AHE**)
These techniques provide information on magnetization orientation, cannot measure the absolute magnetization magnitude, but give a signal roughly proportional to it.

Measurements were performed in the Oxford cryostat, which is a cryogen-free pulse tube cryocooler, working in the (2-300 K) temperature range. The cryostat is equipped with a superconducting magnet (0-7 T), a rotatable sample holder, electrical connections and optical access to the sample through windows.

2.5.1 Magneto Optical Kerr Effect (MOKE)

MOKE measurements were performed on as grown films. MOKE relates to the rotation of the light polarisation and the change of its ellipticity when it is reflected by a magnetic material.

Depending on the orientation of light propagation, with respect to magnetization, MOKE experiments can be:

- **Polar MOKE** Magnetization perpendicular to the reflection surface and parallel to the plane of incidence.
- **Longitudinal MOKE** Magnetization is parallel to the reflection surface and the plane of incidence.
- **Transversal MOKE** Magnetization is parallel to the reflection surface and perpendicular to the plane of incidence

In our case, given that FGT is known to have a strong perpendicular anisotropy, measurements were performed in the **Polar MOKE** configuration, which is only sensitive to perpendicular magnetization component, fig: 2.7.

MOKE setup

The plane of incidence is yz, the sample surface is parallel to xy plane. We define positive magnetic fields along +z direction. The laser generates a beam, which is linearly polarized along x by the first polarizer.
The polarized light then passes through a beam splitter, partially transmitting, and partially reflecting the polarized laser beam to the sample surface.
The beam interacting with the sample is reflected, and is partially transmitted through the beam splitter. Then is it reflected by a mirror and focused with an optical lens on

the photodetector. Before reaching the detector, the focused beam passes through a photo-elastic modulator (PEM).
The PEM retardation amplitude between the E_x and E_z electric field components of light is set at $\theta_0 = 140°$.
The analyser (the polarizer before the detector) is rotated 45° with respect to the PEM axis, which is oriented along x and z.
The conbination of PEM and analyser allows to separate the signal into the Kerr ellipticity ϵ_s and the Kerr angle θ_s. The constant (DC) signal measured with the detector corresponds to the reflected light intensity I_0.

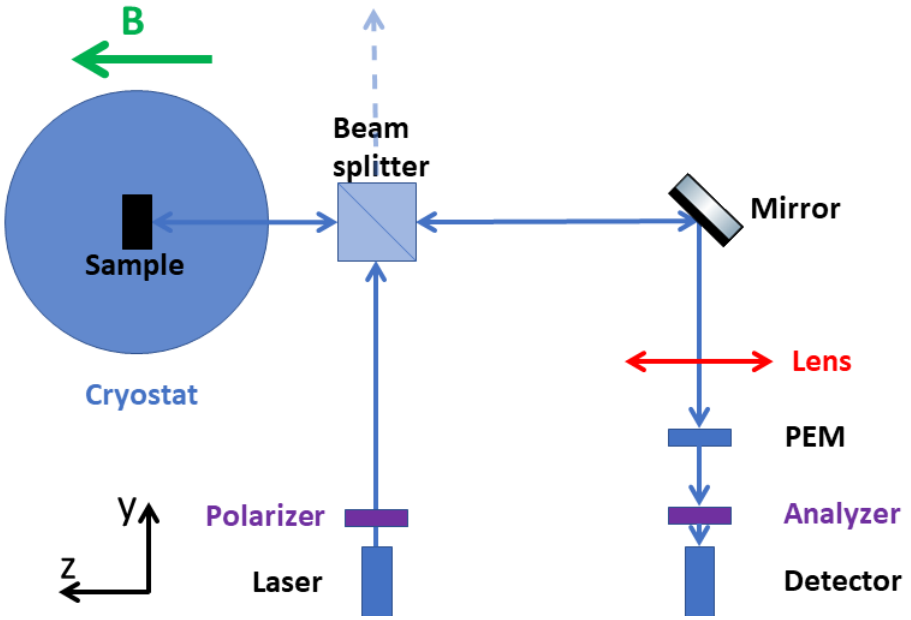

Figure 2.7: Polar MOKE experiment setup

2.5.2 Hall effect and anomalous Hall effect (AHE)

Ordinary Hall effect (OHE)

Ordinary Hall effect occurs in presence of an external magnetic field (along z), describes the presence of an electric field in the transverse direction (along y) when a current is applied in a conductor(along x).
The current, in presence of the applied electrical and magnetic fields $\mathbf{E} = E_x$, $\mathbf{B} = B_z$ is subjected to the Lorentz force The Lorentz force will lead to charge accumulation at surfaces, thus also transverse potential.

We can define the Hall coefficient:

$$R_H = \frac{E_y}{j_x B} = \frac{1}{nq}$$

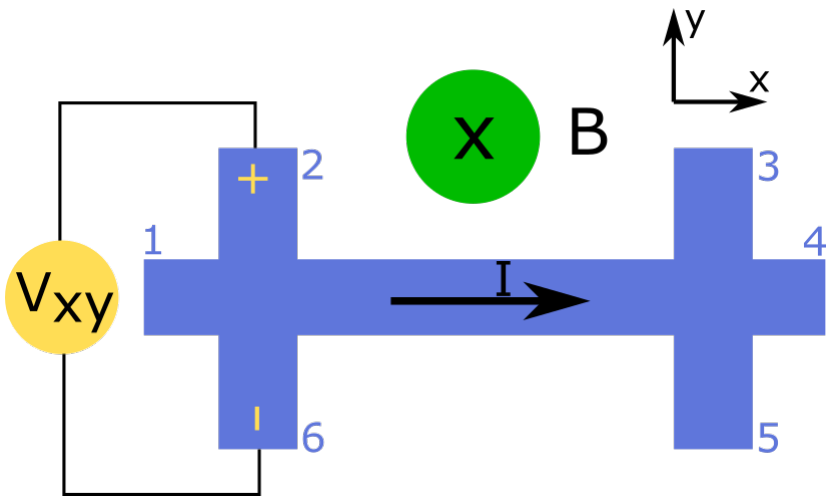

Figure 2.8: Hall bar device. The current I is applied between contacts 1 and 4. The Hall voltage v_{xy} is measured between contacts 2 and 6. The magnetic field B is applied perpendicular to the device plane.

Ordinary Hall effect has been widely used to determine the carrier type in semiconductors, as it determines the polarity of the Hall voltage.
As seen in the formula, the Hall voltage is inversely proportional to the carrier density. It is generally very small in metals, but easily measurable in semiconductors.

Fig: 2.8 depicts a possible geometry to measure Hall effect.
The film is patterned into a *Hallbar* structure, having six electrical contacts.
Injecting a positive continuous current I across contacts 1-4, the Hall voltage V_{xy} is measured across contacts 2-6. Taking into account device dimensions, we can relate R_H, V_{xy} and I.

$$R_H = \frac{E_y}{j_x B} = \frac{V_{xy} d}{IB}$$

where d is the device thickness.

Anomalous hall effect (AHE)

In ferromagnetic materials, in addition to the ordinary Hall effect (OHE), the anomalous hall effect is present. AHE depends on the magnetization, and it is often much larger than ordinary hall effect. Thus, hall resistivity can be expressed in the form:

$$\rho_{xy} = R_H H_z + R_s M$$

where the first term is the contribution of ordinary hall effect, $R_H = \frac{1}{nq}$, R_s are the ordinary and anomalous Hall coefficients, H_z the applied magnetic field, M is the magnetization.

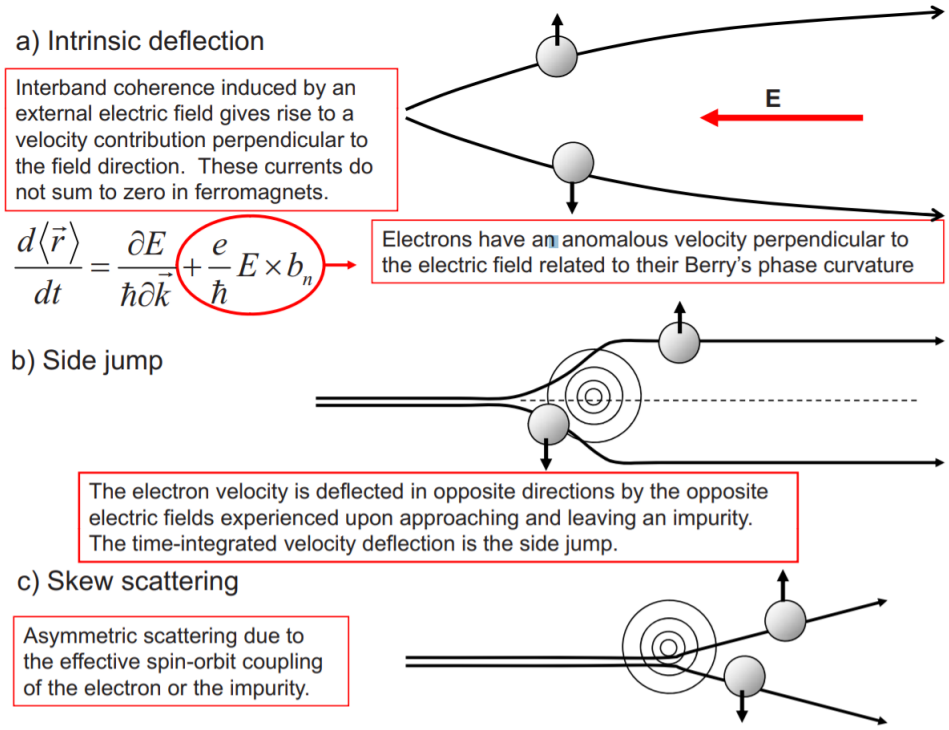

Figure 2.9: Main AHE mechanisms, from [23]

The microscopic origin of AHE is not fully understood. As briefly shown in fig: 2.9, the main known mechanisms are:
Intrinsic effects: Arising from topological considerations, described by Berry phase in k-space, Extrinsic effects: Spin dependent scattering of carriers, e.g. side jump, skew scattering.

Subtracting the contribution OHE, AHE experiments can be used as an indirect measure of the magnetic properties of a film.

CHAPTER 3

Experimental results

3.1 Calibration of the MBE cells

In MBE effusion cells and e-beam evaporation are used to sublimate/evaporate ultrapure materials from solid phase. To achieve good control over fluxes, these must be well calibrated, i.e.

- **For effusion cells**, we must determine the cell temperature/deposition rate relation, as well as the relationship cell temperature/partial pressure of the evaporated material.
- **For e-beam evaporation**, it consists in determining the relationship deposition rate on the quartz crystal microbalance (QCM)/deposition rate on sample.

The partial pressure can be measured right before each growth, to correct the cell temperature if we ever notice some drift, which for instance can occur as source materials are consumed.

3.1.1 Fe calibration

Concerning iron calibration deposition rate is monitored in real time by means of a quartz crystal microbalance (QCM).
Since the QCM and the sample are in a different positions, a geometrical factor (tooling factor) must be taken into account to relate the amount of material deposited on QCM with the flux imping on the substrate.
Hence a calibration is required to correctly measure the amount of Fe impinging on the sample. To obtain this factor, the value measured by the QCM was compared with the actual Fe thickness deposited, which has been measured by X-ray reflectometry (XRR).

X-ray reflectometry exploits diffraction on interfaces, as in fig: 3.1.
The interference of the X-ray beams partially reflected at every interface produces

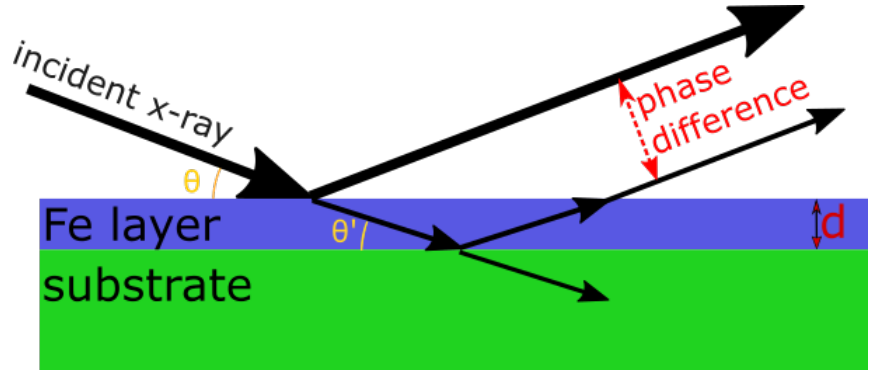

Figure 3.1: XRR measurement

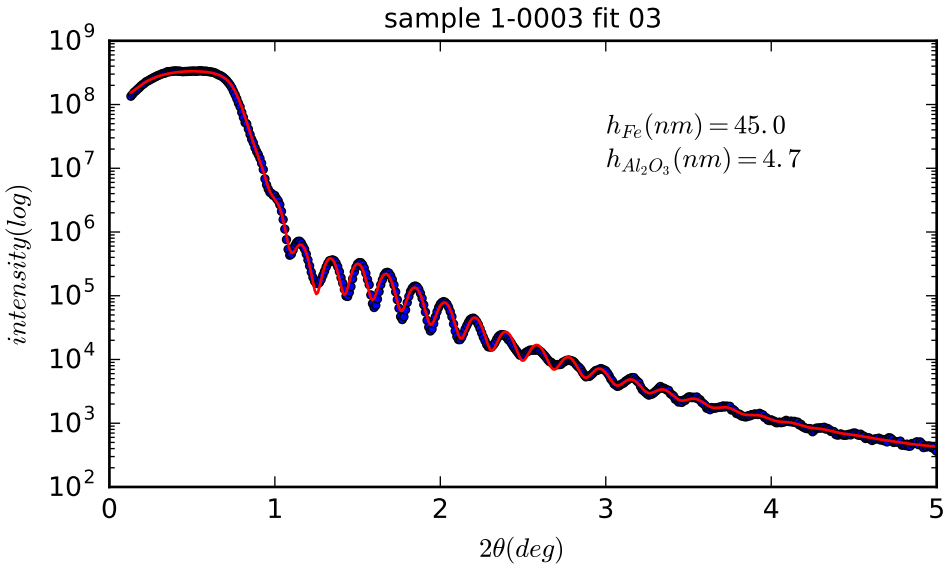

Figure 3.2: XRR measured intensity (black), with fitting (red)

intensity oscillations when the incidence angle is varied, as in fig: 3.2. Using Bragg's law it is possible to estimate the thickness of the film. We grow on a Si/SiO2 substrate an Fe layer and record the QCM reading: 20nm. A thin Al capping layer of known thickness is deposited on Fe layer to prevent oxidation, because e-beam deposition of Al had been previously calibrated.
Measuring with XRR, we obtain the value of the actual thickness 45nm, (fig:3.2).
The result of the calibration is that the QCM reading underestimates the deposition rate by a factor 2.3 (the "tooling factor").

3.1.2 Ge calibration

Ge deposition rate was obtained by measuring RHEED oscillations [24].
Performing homoepitaxial Ge growth, if temperature is not too high i.e. no step flow growth, it is possible to observe intensity of rods oscillate as the growth goes on: fig: 3.3.

In the simplest interpretation, intensity maxima are related to a completion of a monolayer (ML), while minima are related to an incomplete coverage of the surface.

It is easy to estimate the growth rate by measuring the periodicity of oscillations occur while performing Ge homoepitaxy at different cell temperatures. Considering the time intervals between peaks, we can assign an equivalent number of completed ML.
The growth con occur in monolayer or bilayer mode, affecting the period of RHEED oscillations.
In fig:3.3 RHEED intensity oscillation at $T_{Ge} = 1050°C$ are shown. The first dashed vertical line is in correspondence of the start of the growth. Black vertical lines are in correspondence of maxima, the number reported next to each line is the corresponding equivalent number of ML grown.
The growth occurs in monolayer or bilayer mode:
initially ($t < 200s$) monolayer mode growth can be observed, were the time interval between the first two maxima is approximately half of the following ones.
For this reason, maxima 4, 6, 8, 10 are not reported, because they could not be observed in bilayer growth mode.
At $t = 1800s$ the Ge cell shutter is closed, stopping the growth.
Plotting the number of ML against the elapsed time; in fig: 3.4 the slopes of linear fitting allow us to estimate the time required to grow a ML t_{ML} at the given cell temperature:
at $T_{Ge} = 1100°\ C$: $t_{ML}(1100°C) = 25.2\ s$,
at $T_{Ge} = 1075°\ C$: $t_{ML}(1075°C) = 47.0\ s$,
at $T_{Ge} = 1050°\ C$: $t_{ML}(1050°C) = 78.4\ s$.

Finally, it is also useful to correlate the growth rate with the measured pressure: shows a good linear relationship between the two (inset 3.5). Both growth rate and pressure behaviour as a function of T can be modelled using an exponential function $f(T) = a\ e^{-b/T}$.

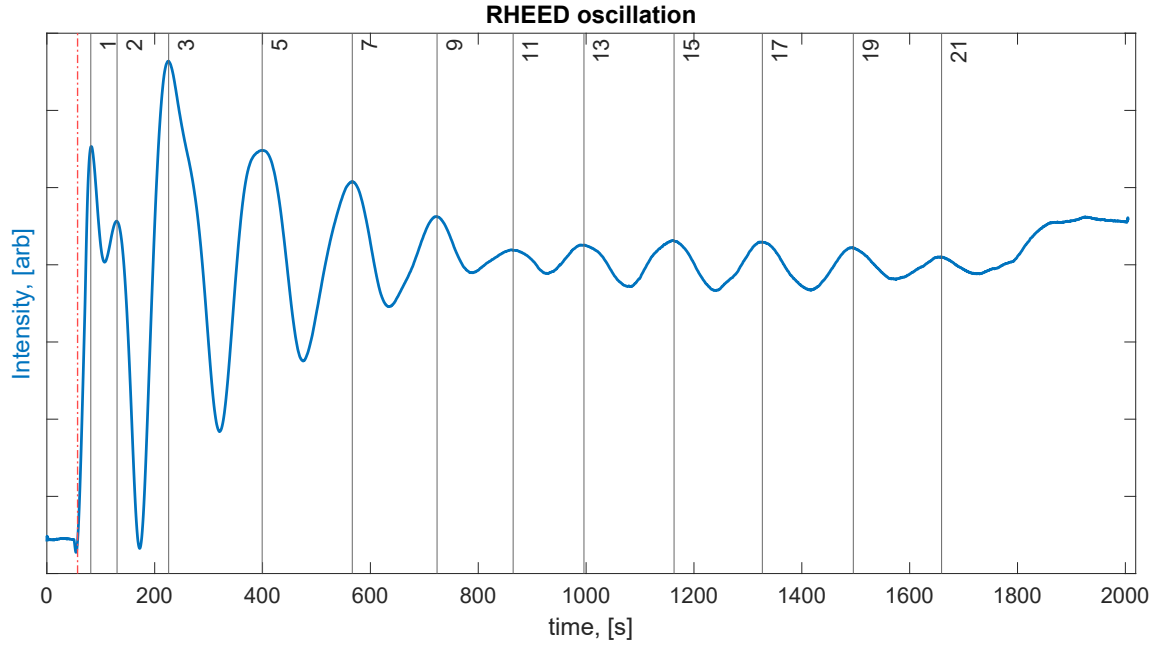

Figure 3.3: Example of measured RHEED intesity oscillation at $T_{Ge} = 1050°C$

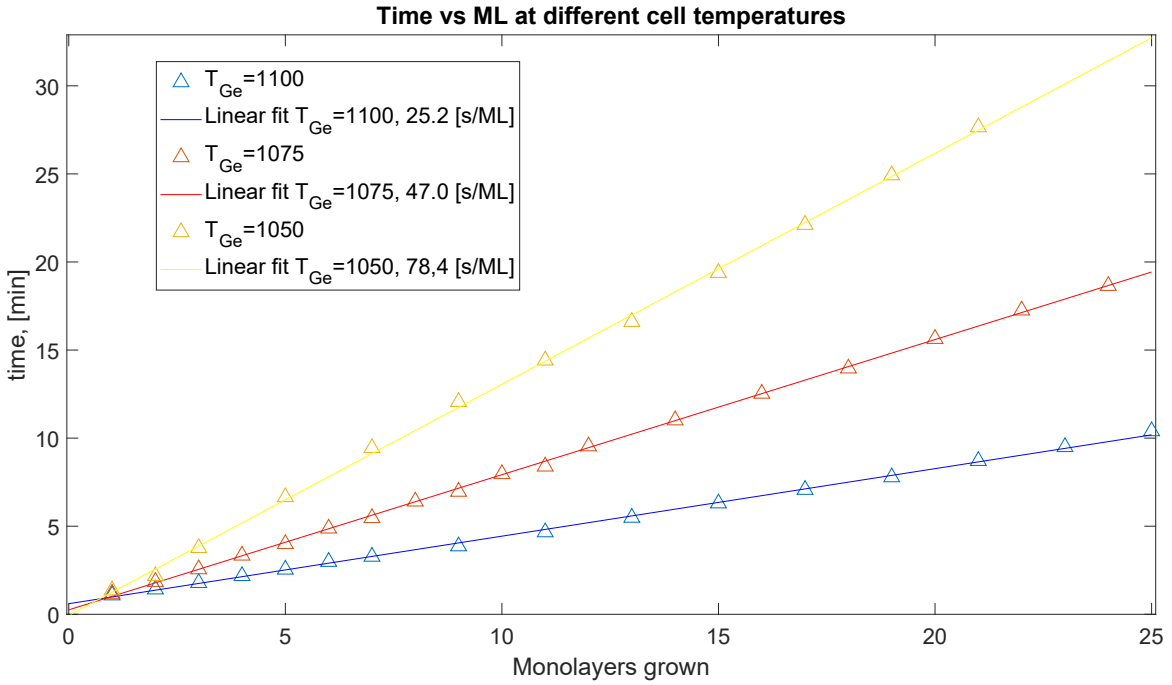

Figure 3.4: Estimation of grow rates of Ge homoepitaxy at different cell temperatures

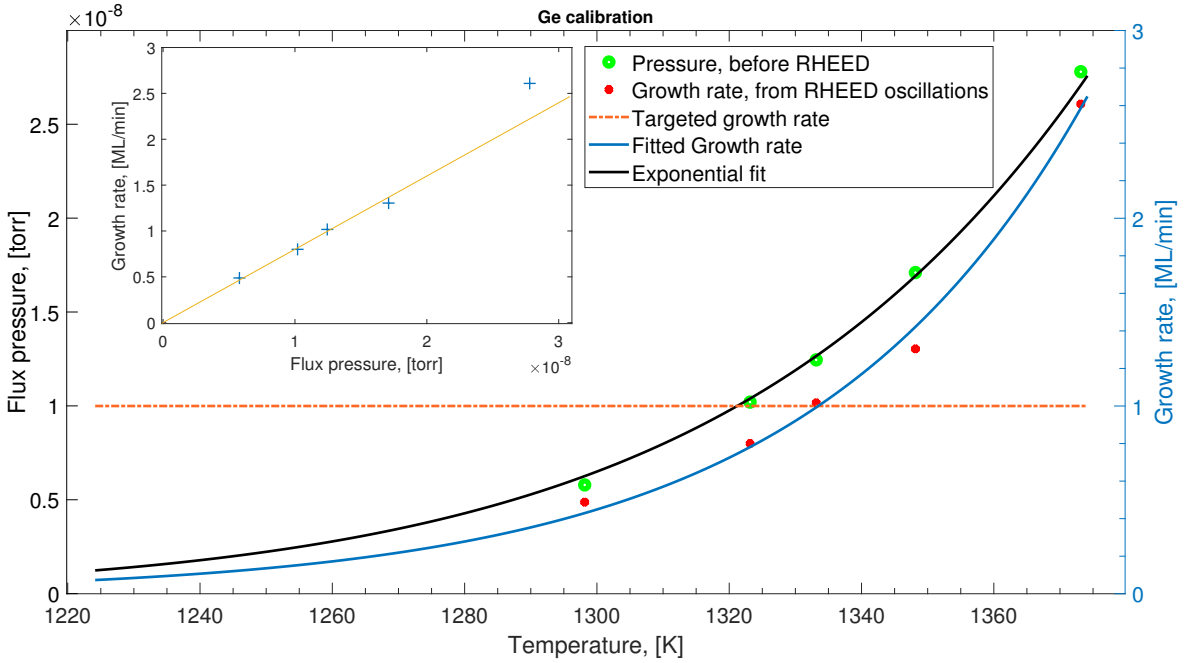

Figure 3.5: Ge calibration: green dots are Ge flux pressures measured by ionization gauge, red points are the growth rate estimated with RHEED oscillations. Black and blue lines are exponential fittings of pressure, and growth rate points, respectively. Inset: plot of growth rate vs pressure points, and their linear fitting.

3.1.3 Te calibration

In the case of Te cell calibration, a series of grooves were first patterned by lithography in a positive resist coated on a Si/SiO2 substrate. After depositing Te, and removing the remaining resist, we performed AFM measurements to measure the step height (3.6), also obtaining the Te growth rate, reported in the following table:

Te cell temperature $°C$	Te tube temperature $°C$	Te cracker temperature $°C$	Growth rate nm/s
290	500	1000	0.0054
315	500	1000	0.0108

Fig: 3.7 shows both pressure and growth rate calibrations for Te. Purple points are the flux pressures as a function of temperature, red asterisks result from the AFM measurements after two growths at $T_{Te} = 563K$ and $T_{Te} = 580K$

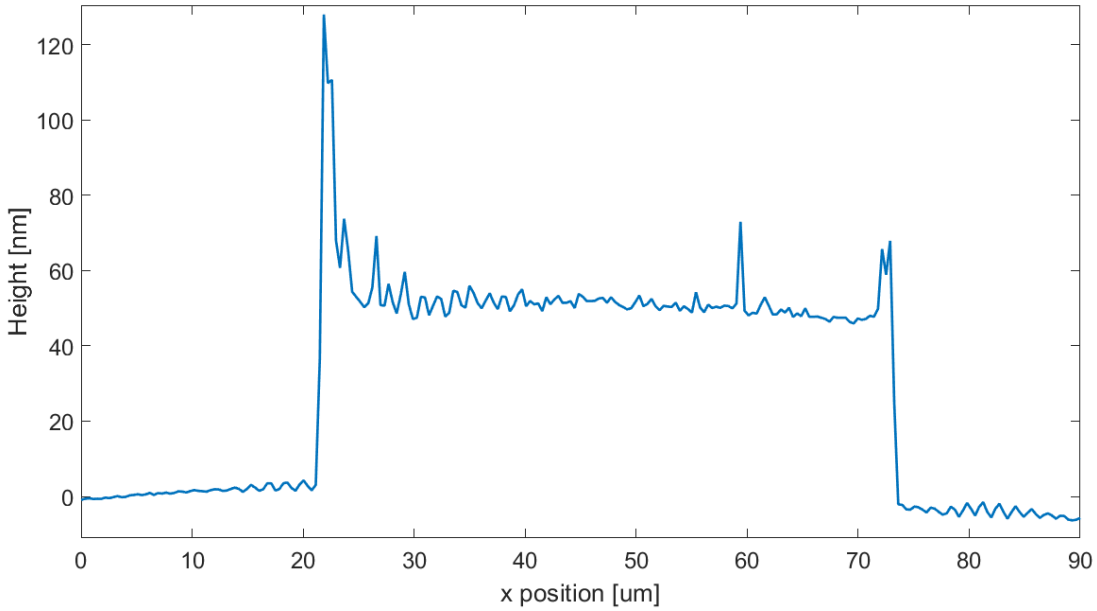

Figure 3.6: Height profile with a step of $\approx 48nm$.

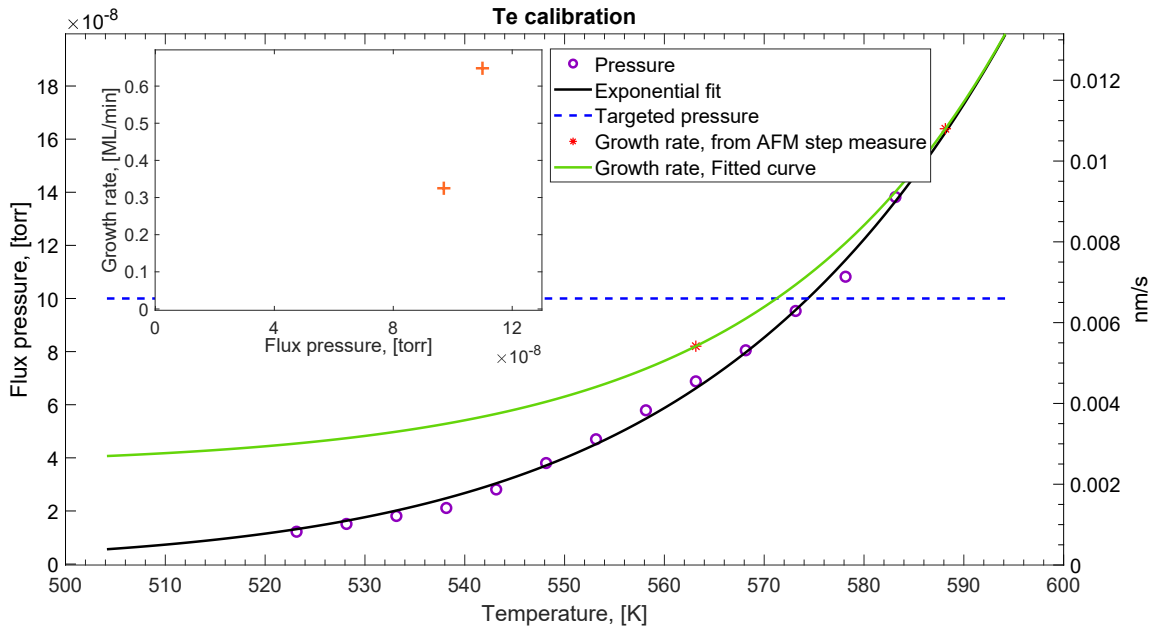

Figure 3.7: Te calibration plot: Purple dots are Te flux pressures measured by ionization gauge, Red points are the growth rate estimated after AFM measurements. Black and green lines are exponential fittings of pressure, and growth rate points, respectively. Inset: plot of growth rate vs pressure points

3.2 Fe_3GeTe_2 growth

3.2.1 Subtrate preparation

We used as substrate Al_2O_3 (0001) surface, as we wanted to first replicate the state of the art results of the only paper on MBE growth of this material [14]. This surface has an hexagonal structure, like Fe_3GeTe_2 (FGT), but with a much larger lattice parameter of $a_{AlO3} = 4,785\mathring{A}$, $\approx 20\%$ larger [25]. The growth can be epitaxial, regardless of the mismatch because of the weak, Van der Vaals nature of interactions of FGT with substrate.
The sapphire substrates were prepared with a procedure already established for a long time in the laboratory, in order to obtain a more continuous surface for the growth. First cut with a diamond tool, they were immersed in acetone, and put in an ultrasonic bath for 5 minutes. Then, without letting dry the polished surface from acetone, sample was moved into isopropanol and again in the ultrasonic bath for 5 minutes. Finally, the sapphire was annealed for $\approx 1h$ at $T = 1050°C$ in air.
AFM images after the annealing show a surface with presence of damage, in form of uniformly distributed dips but featuring more regular terraces, i.e. a smoother surface, more suitable for epitaxial growth.

Once the sapphire substrate is introduced into the UHV growth chamber, it is first

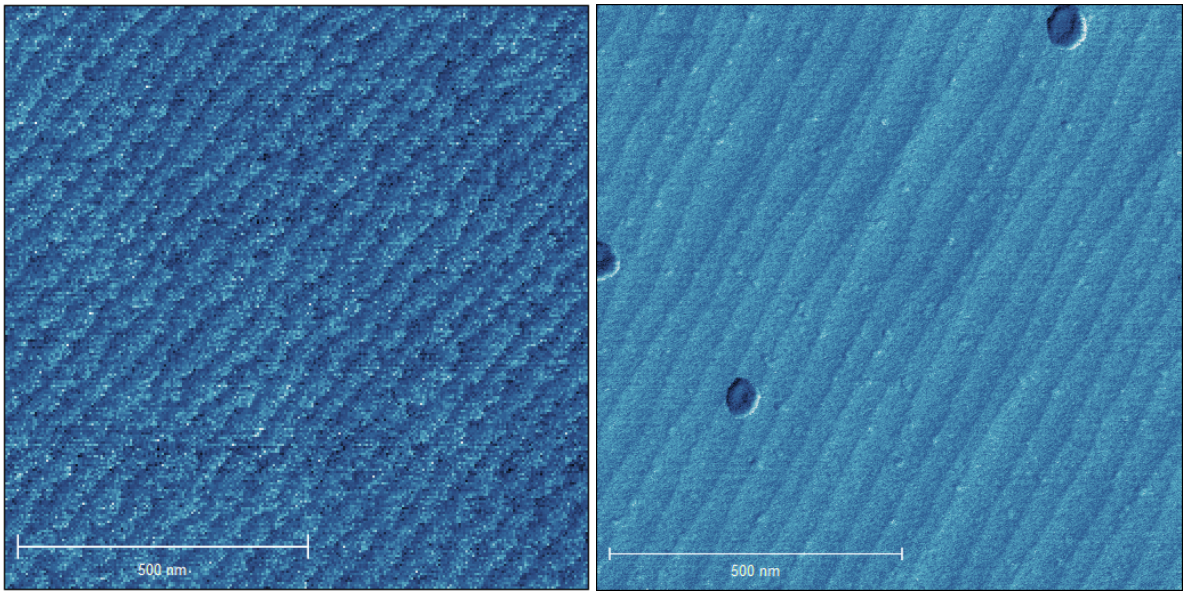

(a) Sapphire surface before annealing (b) Sapphire surface before annealing

Figure 3.8: AFM images of sapphire surface, scale bar is $500nm$

necessary to perform an annealing, ramping up substrate temperature in 30 mins to $T_{sub} = 800° C$, annealing for 30 mins, then cooling down in $\approx$ 40 mins, in order to evaporate adsorbed gaseous impurities on the surface.

3.2.2 Estimation of nominal growth parameters

Targeting a growth rate of 1 ML/min of Fe_3GeTe_2, we can have a first estimation of the fluxes and cell parameters . We can first define some quantities involved in the growth:

The **growth rate** v is the thickness h deposited per unit time t: $v = \frac{h}{t}$
The **atomic density** d is the number of atoms N per unit volume V: $d = N/V$
The **flux of atoms** Φ is the number of atoms N per unit area and unit time t: $\Phi = \frac{N}{At} = dv$
d_{FGT} is the atomic density of FGT (number of unit formulas per unit volume or equivalently, number of Ge atoms per unit volume).
The hexagonal FGT cell with lattice parameters a (in-plane) and c (out-of-plane) contains n unit formulas (n=2 for Fe_3GeTe_2), therefore:

$$d_{FGT} = \frac{2n}{3\sqrt{3}a^2c}$$

For the lattice parameters, we can consider the literature values: $a = 3.99\mathring{A}$, $c = 16.33\mathring{A}$
Noting that there is one Ge atom per FGT formula: $\Phi_{FGT} = \Phi_{Ge}$
the growth rate of FGT (in nm/min):

$$v_{FGT} = \Phi_{FGT}/d_{FGT} = \Phi_{Ge}/d_{FGT} = \frac{3\sqrt{3}}{2n}a^2c\ d_{Ge}v_{Ge}$$

Given that the thickness of 1 FGT monolayer (ML) is c/n, the growth rate $\overline{v}_{FGT}$ in ML/min is:

$$\overline{v}_{FGT} = \frac{v_{FGT}}{c/n} = \frac{3\sqrt{3}}{2}a^2\ d_{Ge}v_{Ge}$$

We can use mass densities d' expressed in g/cm^3, $d' = d \times m \times m_u$, where $m_u \approx 1.66110^{-24}g$ is the atomic mass unit, m the relative atomic mass.
For a targeted growth rate of FGT $\overline{v}_{FGT}$:

$$v_{Fe}[nm/min] = x\frac{2}{3\sqrt{3}}\frac{m_{Fe}m_u}{a^2d'_{Fe}}\overline{v}_{FGT} \tag{3.1}$$

$$v_{Ge}[nm/min] = \frac{2}{3\sqrt{3}}\frac{m_{Ge}m_u}{a^2d'_{Ge}}\overline{v}_{FGT} \tag{3.2}$$

$$v_{Te}[nm/min] = y\frac{2}{3\sqrt{3}}\frac{m_{Te}m_u}{a^2d'_{Te}}\overline{v}_{FGT} \tag{3.3}$$

$$\tag{3.4}$$

where d' are the mass densities expressed in $\frac{g}{cm^3}$.
With $\overline{v}_{FGT} = 1$ ML/min we find:

$$\begin{aligned} v_{Fe} &= 0.2567 \quad \text{nm/min} \\ \overline{v}_{Ge} &= 1.0008 \quad \text{ML/min} \\ v_{Te} &= 0.4917 \quad \text{nm/min} \end{aligned}$$

From our Ge (fig: 3.5) and Te (fig: 3.7) calibrations, we find that these growth rates correspond to $T_{Te} = 580K \approx 307°C$ for Te cell and $T_{Ge} = 1335K \approx 1062°C$ for Ge cell.

3.2.3 Growth procedure

After calibrating the effusion cells, and e-beam evaporators, we estimated the expected material fluxes.
With the nominal conditions given above, we started the the growth tests (sample 1-0011), checking the RHEED pattern to know if the crystal grows correctly. To perform the growth, a specific procedure is followed:

1. Degassing of substrate, described in section 3.2.1.
2. Cell warm up and temperature stabilization for 30min.
3. Check of Te and Ge beam pressures.
4. RHEED alignment
5. Start of deposition by opening all shutters at once
6. Periodically capture the RHEED patterns
7. End of deposition by closing the shutters
8. Post-growth annealing, with/without Te shutter open

In a second step, we fine tune the growth parameters (cells, substrate temperatures, annealing) to improve the crystalline quality.
Table 3.1 below lists all the samples and associated growth parameters. With samples 1-0012,1-0013 and 1-0014 we investigate the effect of substrate temperature, the thicker $\approx 20nm$ sample 1-0019 was used for XRD measurements. With sample 1-0020 we tried a two step growth method, involving an early annealing of the first two layers before continuing with the growth at higher substrate temperature.

In the next sections, we detail our results and discuss separately the influence of these different parameters.

Sample	T_{Ge} $^{\circ}C$	T_{Te}cracker $^{\circ}C$	T_{Te}tube $^{\circ}C$	T_{Te}cell $^{\circ}C$	targeted Fe rate $\mathring{A}$/s	meas. Fe rate $\mathring{A}$	T_{sub} $^{\circ}C$	Annealing-up to $^{\circ}C$	Capping
1-0011	1060	1000	500	305	0,43	0,417	350	550	Al
1-0012	1060	1000	500	305	0,43	0,425	350	500	
1-0013	1060	1000	500	305	0,43	0,425	250	700	
1-0014	1060	1000	500	305	0,43	0,426	450	600	
1-0015									
1-0016 I	1060	1000	500	315	0,43	0,428	350	550	
1-0016 II	1060	1000	500	315	0,43	0,425	400	550	
1-0016 III	1060	1000	500	325	0,43	0,437	350	600	
1-0017									
1-0018	1060	1000	500	315	0,43	0,419	350	500	Al
1-0019	1060	1000	500	315	0,43	0,430	350	550	Al
1-0020	1060	1000	500	305	0,43	0,417			

Table 3.1: Table of FGT samples grown

3.2.4 Substrate temperature

Substrate temperature is a key parameter in epitaxial growth. The optimal value depends on the type of substrate and type of film is desired, it strongly affect the absorption and desorption rate, mobility of adatoms on surface. Samples 1-0012, 1-0013 and 1-0014 were grown to define rough temperature limits where growth starts to be not epitaxial anymore.

Fig: 3.9 shows RHEED patterns of samples 1-0012, 1-0013 and 1-0014, grown respectively at T_{sub} of 350, 250, 450 $°C$. As described in section 2.2, the patterns can be interpreted to gain insight on the nature of the surface.
On the left side we have the patterns of the as grown films: In fig: 3.9a is the RHEED pattern of sample 1-0013, grown at 250 $°C$. Only broad rings are present.
In the RHEED pattern of sample 1-0012, grown at 350 $°C$, fig: 3.9c those rings are less present and even if not very sharp, diffraction rods can be noticed.
In fig: 3.9e the RHEED pattern of sample 1-0012, grown at 450 $°C$, shows dots instead of rods. These features can be interpreted in the following way:

At 250$°C$, broad ring are a sign of a polycrystalline surface, where structure has no preferred orientation. If the sample is rotated, the pattern remains the same.
At 350$°C$,the rods denote a crystalline surface. At 450$°C$, the surface is not flat, and we have the presence of islands. The darker spots are a result of some bulk diffraction, due to electrons penetrating into those islands.
Comparing the as-grown with the patterns after post-growth annealing on the right, we can see as general improvement in the cases of 1-0013 fig: 3.9b and 1-0012 fig:3.9d, because the surface is able to reconstruct and form a single crystal.

The same improvement does not occur for 1-0014 fig: 3.9f. A possible explanation is that the higher growth temperature might reduce the presence of Te, altering the stoichiometry and structure of the film, which is not able to form a flatter surface.

We conclude that growth with substrate temperature $T_{sub} = 350°C$, followed by annealing at $T_{sub} = 550°C$ to be optimal.

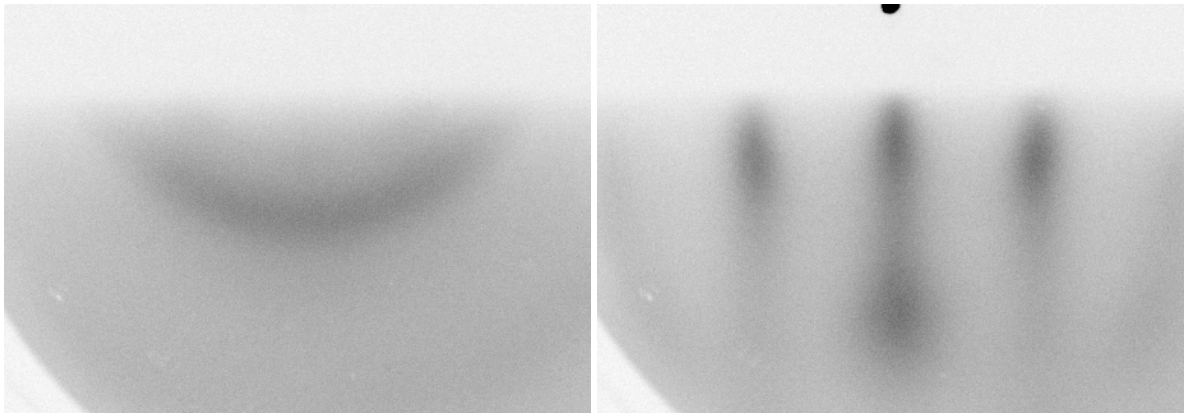

(a) 1-0013 as grown

(b) 1-0013 after annealing

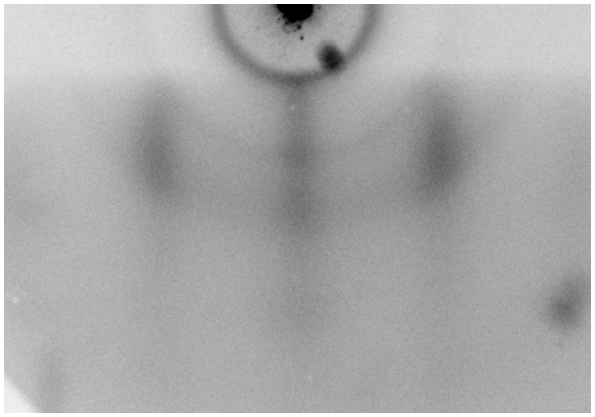

(c) 1-0012 as grown

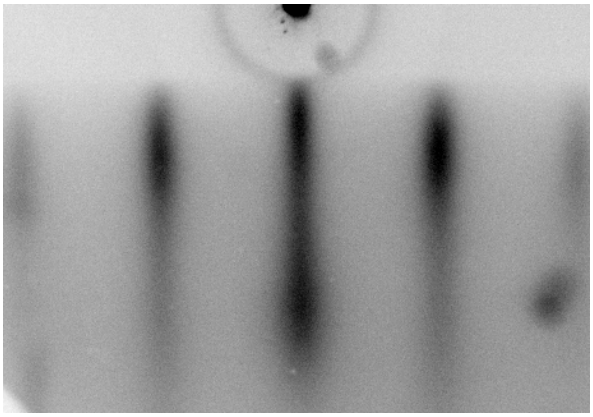

(d) 1-0012 after annealing

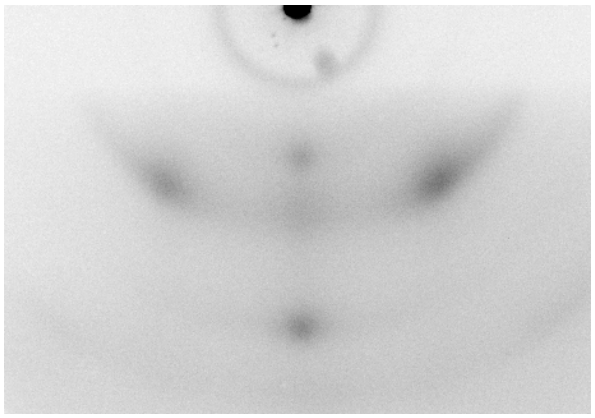

(e) 1-0014 as grown

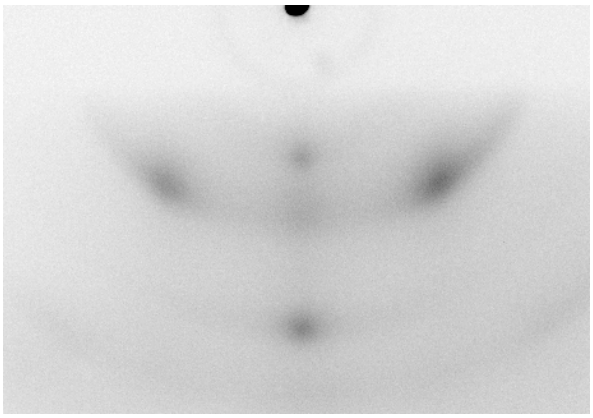

(f) 1-0014 after annealing

Figure 3.9: RHEED patterns of samples 1-0012, 1-0013 and 1-0014, grown respectively at T_{sub} of 350, 250, 450 $°C$, as grown (left side), and after a post-growth annealing

3.2.5 Deposition time dependence

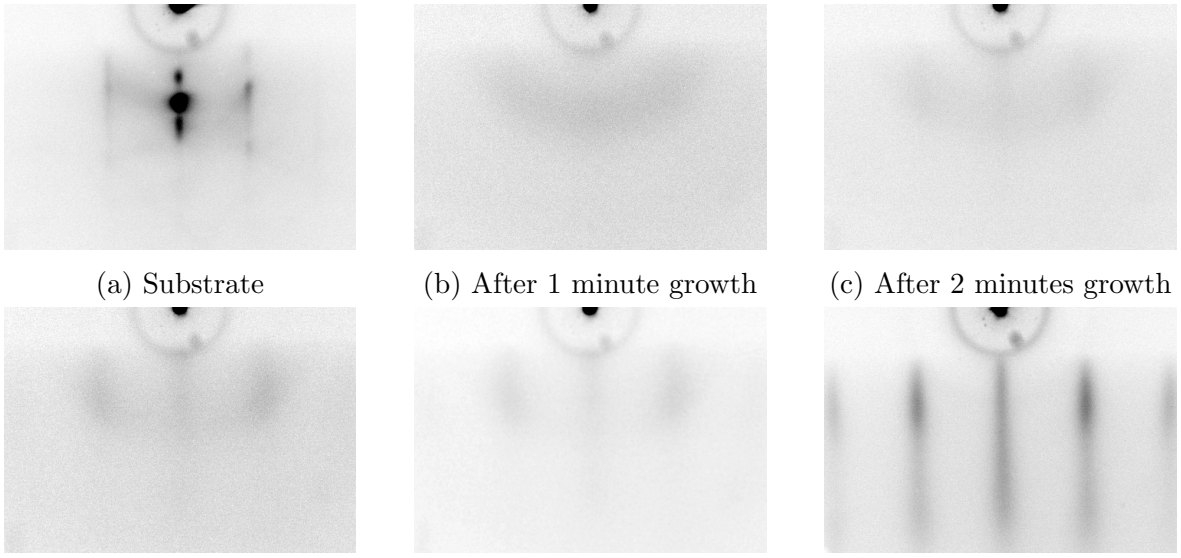

(a) Substrate (b) After 1 minute growth (c) After 2 minutes growth

(d) After 3 minutes growth (e) After 4 minutes growth (f) After 12 minutes growth

Figure 3.10: RHEED patterns of sample 1-0011 acquired at different growth times

Figure 3.10 shows the RHEED pattern evolution of sample 1-00011 as the material is grown at $T_{sub} = 350°C$. The pattern in fig: 3.10a tells how the substrate is monocrystalline, with vertical stripes corresponding to $[11\bar{2}0]$ orientation, diagonal Kikuchi lines arising from the bulk diffraction of electrons.
Shortly after opening Fe, Ge, Te shutters, the surface starts to be covered, and, due to the very short penetration length, we lose the substrate pattern, having no well defined pattern at first (fig: 3.10b), then more contrasted vertical rods after a few minutes (fig: 3.10e), sign of a more crystalline surface.
After the growth of 12 layers (fig: 3.10f) these rods become well defined and contrasted. Other samples gave clear RHEED patterns sooner, probably a sign of better crystallinity of the first layers. In conclusion: the first layer does not have a well-defined crystallinity.
Epitaxy is noticed from the second layer.

3.2.6 Anisotropy of the crystal

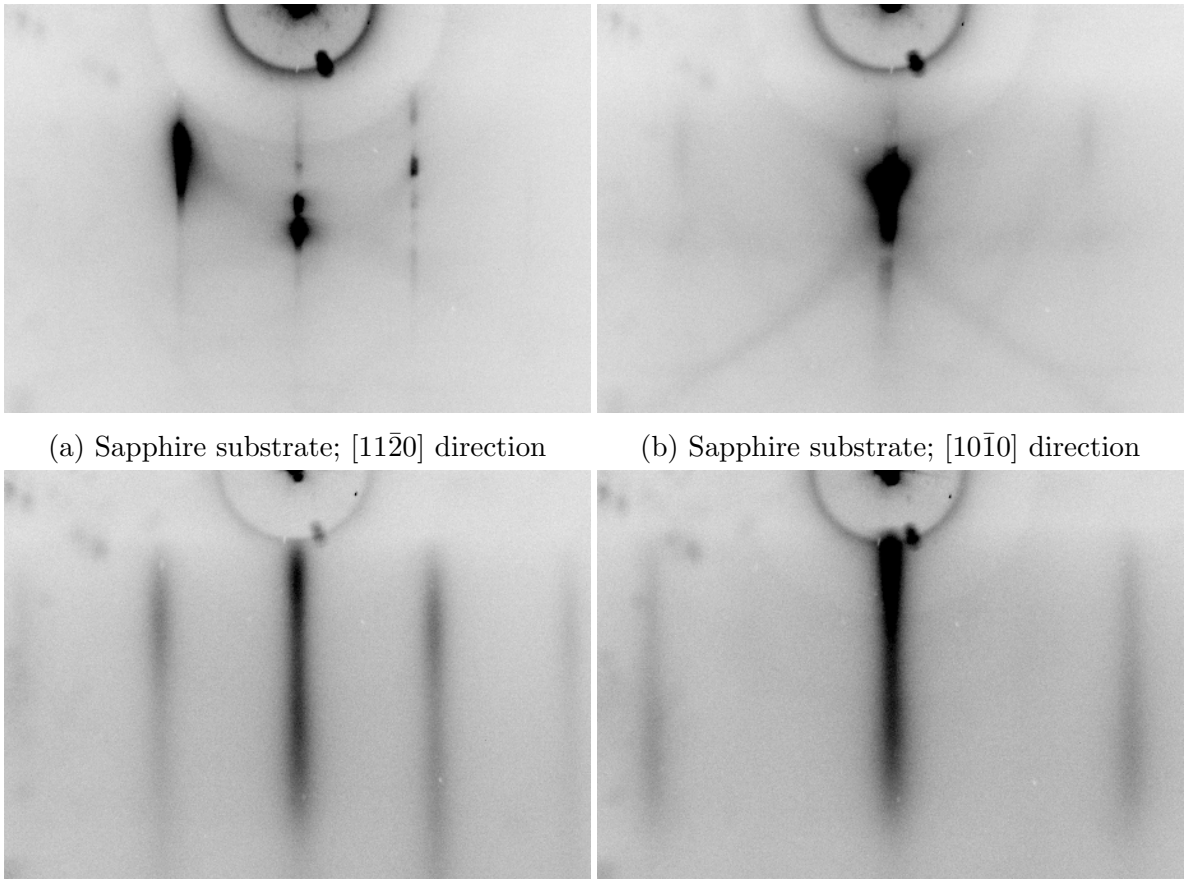

(a) Sapphire substrate; $[11\bar{2}0]$ direction

(b) Sapphire substrate; $[10\bar{1}0]$ direction

(c) FGT; $[11\bar{2}0]$ direction

(d) FGT; $[10\bar{1}0]$ direction

Figure 3.11: Sample 16-I, RHEED pattern of sapphire substrate and of the surface of FGT grown. The given orientations are the crystallographic direction parallel to the electron beam.

Figures 3.11b, 3.11a show good quality of the sapphire subrstrate. The RHEED pattern is anisotropic, showing larger rod spacing for the $[10\bar{1}0]$ direction(opposed to $[11\bar{2}0]$), as in the real space interatomic distance in direction transverse to $[10\bar{1}0]$ is smaller by a factor of $\sqrt{3}$.
It is clear that the film grown shows good crystalline quality, with well defined rods and little intensity modulation; furthermore, the pattern is distinctly anisotropic. Lattice rod distance is inversely proportional to the lattice constant. We can have a first, rough estimation of FGT lattice parameter from the RHEED patterns of fig: 3.11 by taking the ratios of rod distances of FGT and Al_2O_3 multiplied by Al_2O_3 lattice constant. For instance, in fig:3.11a Al_2O_3 *rod distance* $= 91 pixel$, in fig: 3.11c *FGT rod distance* $=$

$108 pixel$, then

$$a_{FGT} = \frac{Al_2O_3 \ rod \ distance}{FGT \ rod \ distance} a_{Al_2O_3} = \frac{91}{108} 4.785 \mathring{A} = 4,0318 \mathring{A}$$

Which is close to the XRD result of $4,07 \mathring{A}$

3.3 Structural characterization with XRD

XRD measurements provide a more quantitative structural characterization compared to RHEED.
Three measurements were done by choosing different azimuthal angles of the sample Φ, (fig: 3.12).
Different orientations Φ will give different diffraction intensities if the sample is anisotropic.
It is possible to first notice peaks related to the Al_20_3 substrate, which has good crystallinity, and its pattern is clearly anisotropic as we scan $2\Theta_{//}$.
The blue and red curves show peaks related to FGT structure, changing Φ the peaks change, proving the FGT diffraction pattern anisotropic;
However, the sample is not completely anisotropic, as some peaks, in particular FGT (110) are still present even at $\Phi = 0°$, $\Phi = -15°$, and may indicate the presence of misaligned domains in surface film structure.

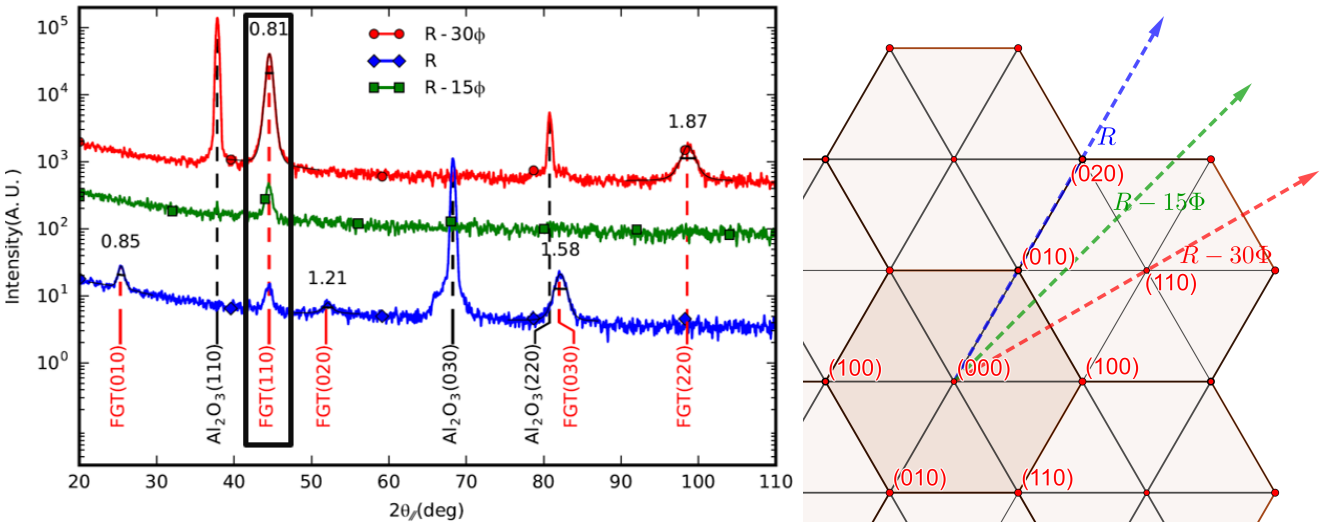

(a) XRD measurements

(b) XRD scans in reciprocal lattice

Figure 3.12: XRD measurements. a) XRD scans at $\Phi = -30°$(red), $\Phi = 0°$ (blue), $\Phi = -15°$(green). Peaks related to Al_2O_3, as well as FGT are present. The peak FGT(110) in the rectangle should be absent at $\Phi = -15°$ and $\Phi = -30°$ for an ideal crystal. b) Shows the three corresponding paths in the reciprocal space. Crossing a reciprocal lattice point corresponds to fulfilling diffraction condition.

We can estimate the lattice parameter of FGT from XRD results:
$a_{FGT} = 4,07\mathring{A}$, which is $\approx 1.47\%$ higher than literature value $4.01\mathring{A}$ [25].

3.4 Chemical characterization with XPS

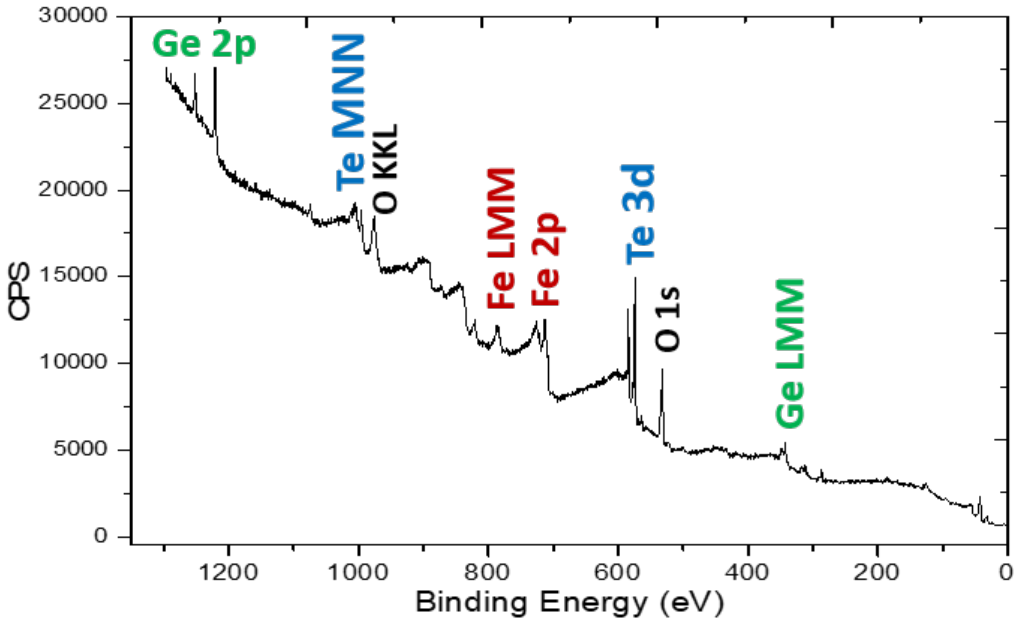

Figure 3.13: XPS spectrum of FGT

XPS chemical characterization, (fig: 3.13) indicates the presence of Fe, Ge and Te. Oxygen peaks are also present, because the sample was exposed to air before the measurement. No other contamination is identified. This spectrum is a reference and will be used in the future when we make heterostructures or if we decide to tune the composition of FGT. To avoid oxidation, it will be interesting to test Te capping before transfer, then decapping by mild annealing prior to XPS measurements.

3.5 Magnetic characterization

3.5.1 Polar MOKE measurements

Sample 1-0011

The following figure (3.14a) shows the behaviour of the raw MOKE signal when varying the external field, with temperature as parameter.

We notice a sizable hysteresis loop at temperatures below 200 K The coercive field (fig: 3.14b) decreases with increasing the temperature, approaching $0mT$ for $T \approx 220K$. These curves indicate the presence of ferromagnetic order and clear perpendicular anisotropy, with Curie temperature roughly around 230 K, as expected from literature. more considerations on fig:3.14a can be made: a slope as a function of the external filed is present and the loops are not symmetrical in positive and negative field. The slope can originate from the Faraday effect of the cryostat windows. It can also be due to some paramagnetic component in the sample signal. We suspect that the asymmetry is due to the alignment of the optical setup. We could reduce it but never suppress it completely.

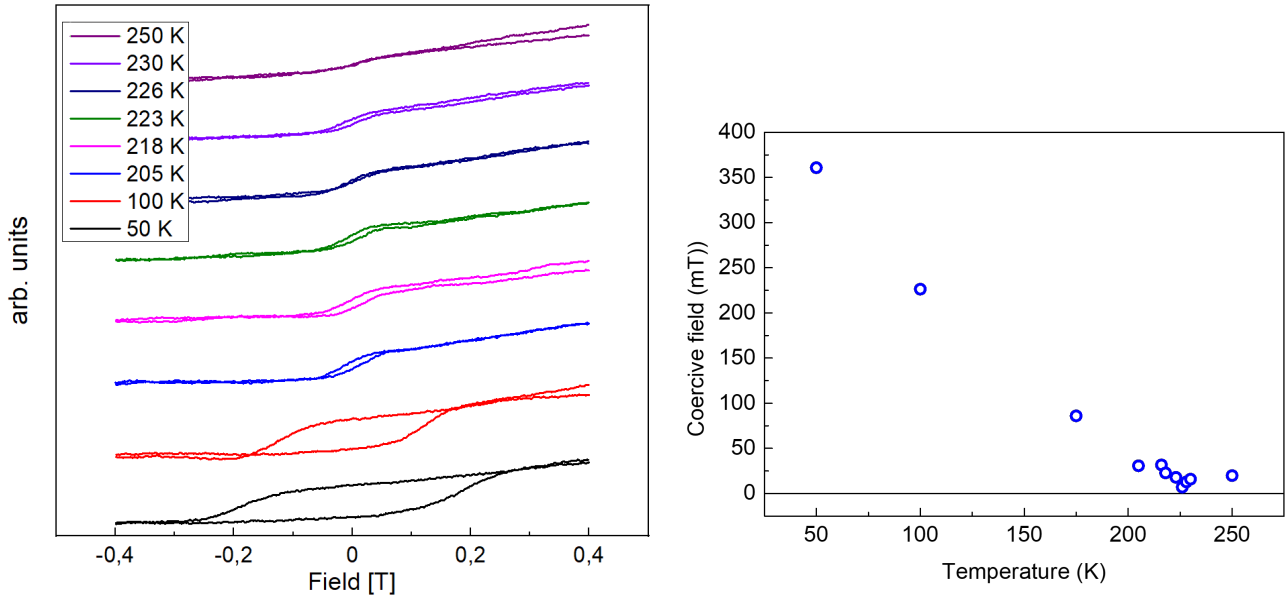

(a) Kerr rotation loops, RAW data. curves are vertically shifted for clarity.

(b) Temperature dependence of the coercive field.

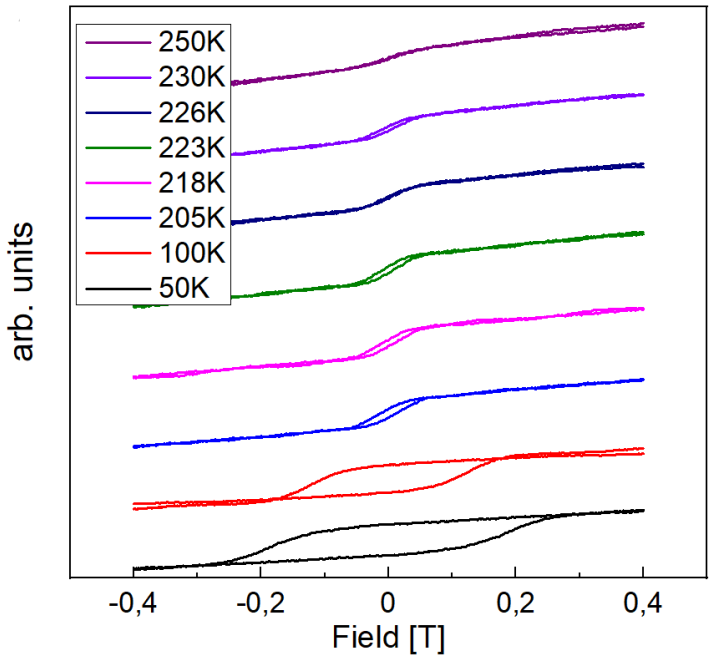

Figure 3.15: Symmetrized MOKE loops after post processing

With some post-processing of the raw data, we can enforce the loops to be symmetric. This was done by writing a Matlab script: the script allows to first read the MOKE data, automatically separate different loops. Then, after choosing the desired loop, is able to symmetrize the loop, by first splitting the loop in four parts as shown in (fig: 3.16a), then interpolating and taking the averages of part 1 and 3; part 2 with 4, respectively. Finally the symmetrized loop is assembled, (fig: 3.16b).

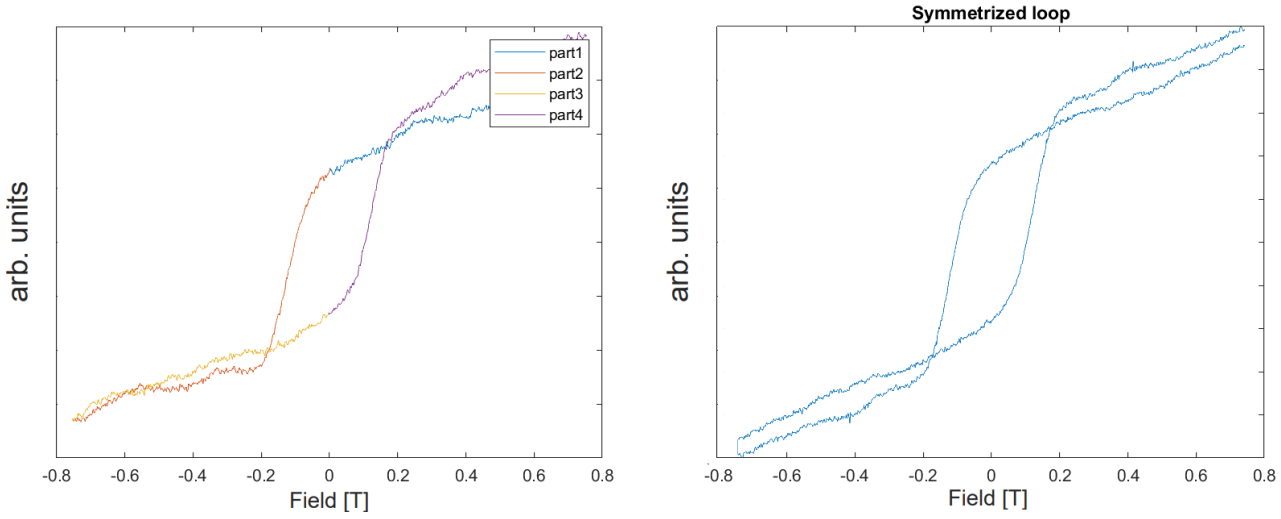

(a) Raw loop, separated into four parts.

(b) Symmetrized loop

Figure 3.16: Field-symmetrization of MOKE loops.

3.5.2 Anomalous hall effect measurements

Definition of Hall bar structure

The Hall bar device is fabricated in two steps:
I: Patterning of the Hall bar by laser lithography: A positive resist is selectively exposed to define the geometry. The resist is then developed, followed by an ion beam etching, for 3'. Then is exposed to oxygen plasma and finally excess material is removed by acetone.
II: Ti/Au electrical contacts are patterned by lift off: A thin $5nm$ thick Ti layer is deposited as adhesion promoter, then a thicker $120nm$ of Au. Then, the excess material is removed by lift off using acetone.

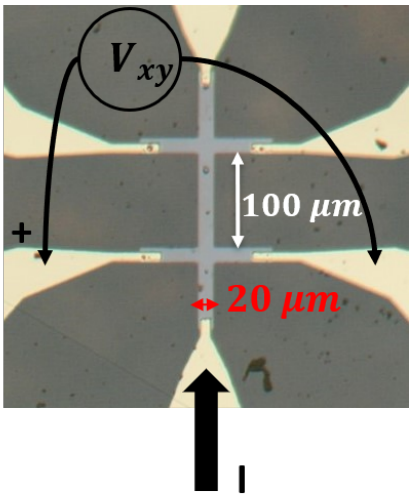

Figure 3.17: Hallbar structure micrograph

AHE measurements

Applying a current in the longitudinal axis, we measure the Hall voltage V_{xy} across, as shown in fig: 3.17.
Performing these measurements in the cryostat, first we choose temperature as parameter, the measure the AHE as the external magnetic field is swept.
The result is shown in fig: 3.18, and essentially agree with MOKE results.

3.5.3 Arrott plot

Arrot plot allows to better determine the Curie temperature of a ferromagnet.
The Arrot plot is a plot of the square of the magnetization M^2, against the ratio of applied magnetic field and magnetization H/M, at different temperatures. According to the Ginzburg–Landau mean field picture for magnetism, the free energy of a

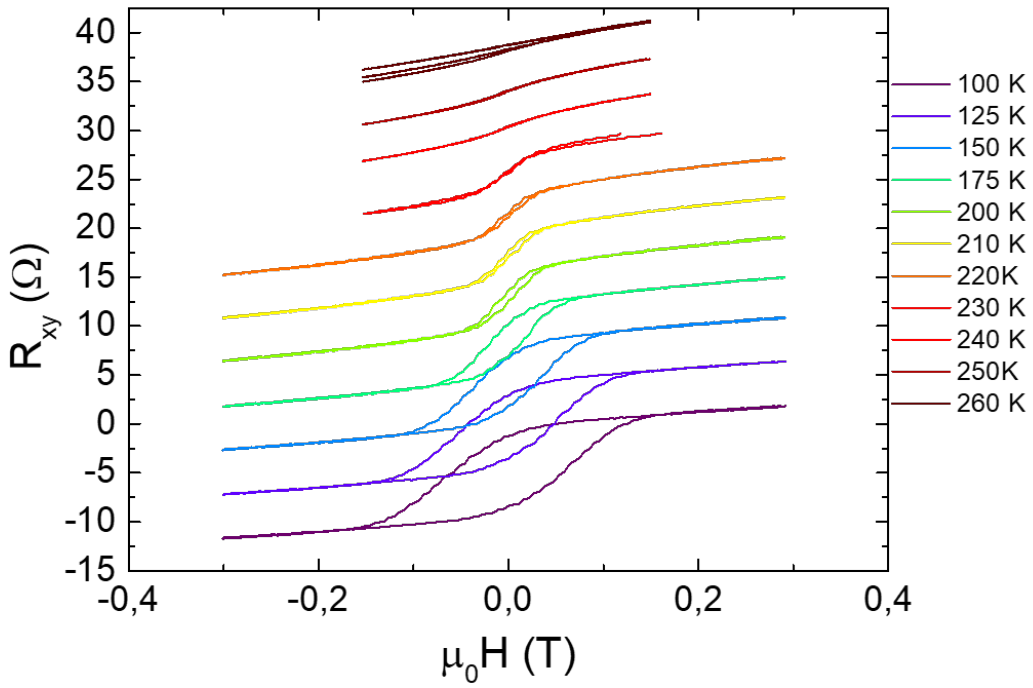

Figure 3.18: AHE loops at different temperatures. The hysteresis is evident below T=200K

ferromagnetic material close to a phase transition can be written as

$$F(M) = -HM + a\frac{T - T_c}{T_c}M^2 + bM^4 + ...$$

where the magnetization M, is the order parameter, T_c the critical temperature, a,b are material specific constants. for $T \to T_c$, we have:

$$M^2 = \frac{1}{4b}\frac{H}{M} - \frac{a}{2b}\epsilon$$

where $\epsilon = \frac{T-T_c}{T_c}$. Taking Linear interpolation of the linear part of the curve M^2 vs B/M, we consider the intercept with the y axis, which should be zero at $T = T_c$. Reporting these intercepts, at different temperatures in another plot, we can interpolate the points that have intercept ≈ 0 to determine the T_c.

Using AHE data, and assuming that we have a signal proportional to magnetization, we can plot R_{xy}^2 vs $\frac{H}{R_{xy}}$ at different temperatures, in fig: 3.19a. The intercepts with y axis were reported in another plot to interpolate fig: 3.19b, estimating a $Tc \approx 234K$, in agreement with literature.

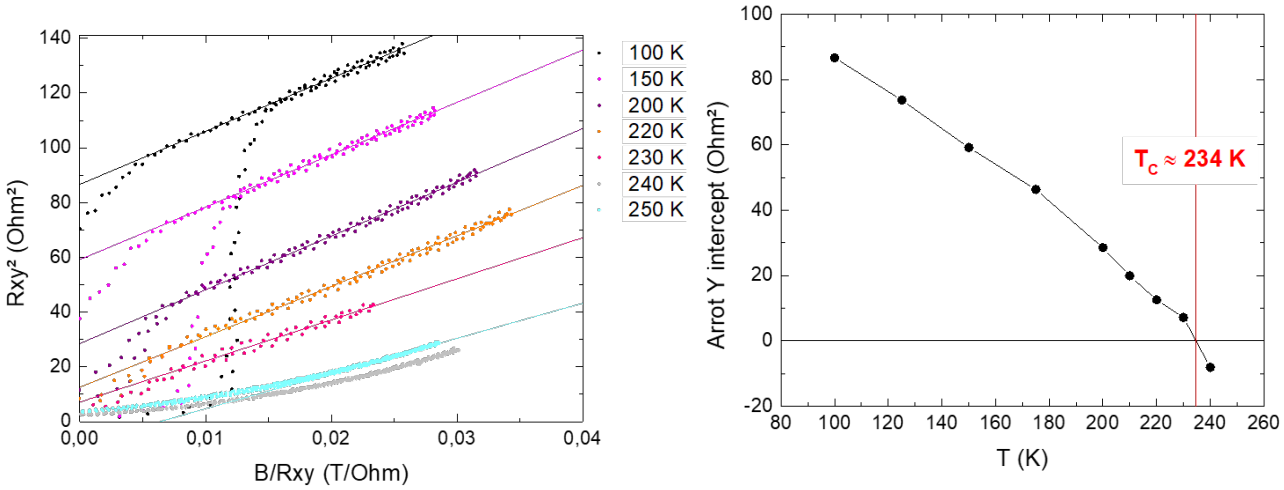

(a) Arrot plot

(b) Arrot plot intercepts

Figure 3.19: Determination of T_c with the Arrot plot.

Conlusions and perspectives

We were able to epitaxially grow Fe_3GeTe_2 (FGT) on sapphire by molecular beam epitaxy (MBE). The experimental results of characterization show structural, chemical and magnetic properties in accord with the only state of the art paper on MBE of FGT. Reflection high energy electron diffraction (RHEED) patterns describe a surface with good structure. The more quantitative x-ray diffraction analysis highlight the presence of mosaicity, but in general agrees with RHEED results. Finally, magnetic measurements with magneto optical Kerr effect and anomalous Hall effect prove the presence of ferromagnetic order with a sizeable magnetocrystalline anisotropy, characterized by a Curie temperature of $Tc = 234K$ for $\approx 12nm$ flakes. cations.

There is still some work planned to further improve the quality of the films and to achieve good FGT down to a single ML. It will then be possible to combine FGT with other vdW materials (TMDs and topological insulators). On the long term, it will be interesting to study spintronics effects (for instance spin orbit torques) in these epitaxial vdW heterostructures.

Acknowledgements

This work has been done in the "2D and semiconductor spintronics" team of Spintec (Univ. Grenoble Alpes/CEA/CNRS). I would like thank all members of the team, particularly my supervisors Frédéric Bonell and Matthieu Jamet as well as Mario Oliveira Ribeiro for their support, but also Thomas Guillet, Alain Marty, Celine Vergnaud and Khasan Abdukayumov.
i must acknowledge contributions in this work by team members: Alain Marty for XRD and XRR measurements, Thomas Guillet for fabrication of Hall bar device and patterning for Te calibration, Khasan Abdukayumov for MOKE and AHE measurements, Mario Oliveira Ribeiro and Frédéric Bonell for their contributions on growth and almost every aspect of this work. My contributions consist on growth of the films by MBE, substrate preparation, AFM measurements and data analysis of magnetic measurements.

Bibliography

[1] K. S. Novoselov et al. "Electric Field Effect in Atomically Thin Carbon Films". In: *Science* 306.5696 (2004), pp. 666–669. ISSN: 0036-8075. DOI: 10.1126/science.1102896. eprint: https://science.sciencemag.org/content/306/5696/666.full.pdf. URL: https://science.sciencemag.org/content/306/5696/666.

[2] Sajedeh Manzeli et al. "2D transition metal dichalcogenides". In: *Nature Reviews Materials* 2.8 (June 2017), p. 17033. ISSN: 2058-8437. DOI: 10.1038/natrevmats.2017.33. URL: https://doi.org/10.1038/natrevmats.2017.33.

[3] Jian Liu et al. "Intrinsic valley polarization of magnetic VSe2 monolayers". In: *Journal of Physics: Condensed Matter* 29.25 (2017), p. 255501.

[4] Yeliang Wang et al. "Monolayer PtSe2, a new semiconducting transition-metal-dichalcogenide, epitaxially grown by direct selenization of Pt". In: *Nano letters* 15.6 (2015), pp. 4013–4018.

[5] Kailiang Zhang et al. "Two dimensional hexagonal boron nitride (2D-hBN): synthesis, properties and applications". In: *J. Mater. Chem. C* 5 (46 2017), pp. 11992–12022. DOI: 10.1039/C7TC04300G. URL: http://dx.doi.org/10.1039/C7TC04300G.

[6] Mazhar N Ali et al. "Large, non-saturating magnetoresistance in WTe 2". In: *Nature* 514.7521 (2014), pp. 205–208.

[7] Yuqiang Ma et al. "Reversible Semiconducting-to-Metallic Phase Transition in Chemical Vapor Deposition Grown Monolayer WSe2 and Applications for Devices". In: *ACS Nano* 9.7 (2015). PMID: 26125321, pp. 7383–7391. DOI: 10.1021/acsnano.5b02399. eprint: https://doi.org/10.1021/acsnano.5b02399. URL: https://doi.org/10.1021/acsnano.5b02399.

[8] Zhiming M Wang. *MoS2: materials, physics, and devices*. Vol. 21. Springer Science & Business Media, 2013.

[9] Takayoshi Yokoya et al. "Fermi surface sheet-dependent superconductivity in 2H-NbSe2". In: *Science* 294.5551 (2001), pp. 2518–2520.

[10] N. D. Mermin and H. Wagner. "Absence of Ferromagnetism or Antiferromagnetism in One- or Two-Dimensional Isotropic Heisenberg Models". In: *Phys. Rev. Lett.* 17 (22 Nov. 1966), pp. 1133–1136. DOI: 10.1103/PhysRevLett.17.1133. URL: https://link.aps.org/doi/10.1103/PhysRevLett.17.1133.

[11] Cheng Gong et al. "Discovery of intrinsic ferromagnetism in two-dimensional van der Waals crystals". In: *Nature* 546.7657 (June 2017), pp. 265–269. ISSN: 1476-4687. DOI: 10.1038/nature22060. URL: https://doi.org/10.1038/nature22060.

[12] J L Lado and J Fernández-Rossier. "On the origin of magnetic anisotropy in two dimensional CrI3". In: *2D Materials* 4.3 (June 2017), p. 035002. DOI: 10.1088/2053-1583/aa75ed. URL: https://doi.org/10.1088%2F2053-1583%2Faa75ed.

[13] Bevin Huang et al. "Layer-dependent ferromagnetism in a van der Waals crystal down to the monolayer limit". In: *Nature* 546.7657 (June 2017), pp. 270–273. ISSN: 1476-4687. DOI: 10.1038/nature22391. URL: https://doi.org/10.1038/nature22391.

[14] Shanshan Liu et al. "Wafer-scale two-dimensional ferromagnetic Fe3GeTe2 thin films grown by molecular beam epitaxy". In: *npj 2D Materials and Applications* 1.1 (Sept. 2017), p. 30. ISSN: 2397-7132. DOI: 10.1038/s41699-017-0033-3. URL: https://doi.org/10.1038/s41699-017-0033-3.

[15] Hans-Jorg Deiseroth et al. "Fe3GeTe2 and Ni3GeTe2 - Two New Layered Transition-Metal Compounds: Crystal Structures, HRTEM Investigations, and Magnetic and Electrical Properties". In: *European Journal of Inorganic Chemistry* 2006.8 (2006), pp. 1561–1567. DOI: 10.1002/ejic.200501020. eprint: https://chemistry-europe.onlinelibrary.wiley.com/doi/pdf/10.1002/ejic.200501020. URL: https://chemistry-europe.onlinelibrary.wiley.com/doi/abs/10.1002/ejic.200501020.

[16] Kyoo Kim et al. "Large anomalous Hall current induced by topological nodal lines in a ferromagnetic van der Waals semimetal". In: *Nature Materials* 17.9 (Sept. 2018), pp. 794–799. ISSN: 1476-4660. DOI: 10.1038/s41563-018-0132-3. URL: https://doi.org/10.1038/s41563-018-0132-3.

[17] Yujun Deng et al. "Gate-tunable room-temperature ferromagnetism in two-dimensional Fe3GeTe2". In: *Nature* 563.7729 (Nov. 2018), pp. 94–99. ISSN: 1476-4687. DOI: 10.1038/s41586-018-0626-9. URL: https://doi.org/10.1038/s41586-018-0626-9.

[18] Mohammed Alghamdi et al. "Highly Efficient Spin–Orbit Torque and Switching of Layered Ferromagnet Fe3GeTe2". In: *Nano Letters* 19.7 (July 2019), pp. 4400–4405. ISSN: 1530-6984. DOI: 10.1021/acs.nanolett.9b01043. URL: https://doi.org/10.1021/acs.nanolett.9b01043.

[19] Andrew F. May et al. “Ferromagnetism Near Room Temperature in the Cleavable van der Waals Crystal Fe5GeTe2”. In: *ACS Nano* 13.4 (2019). PMID: 30865426, pp. 4436–4442. DOI: 10.1021/acsnano.8b09660. eprint: https://doi.org/10.1021/acsnano.8b09660. URL: https://doi.org/10.1021/acsnano.8b09660.

[20] Cheng Gong and Xiang Zhang. “Two-dimensional magnetic crystals and emergent heterostructure devices”. In: *Science* 363.6428 (2019). ISSN: 0036-8075. DOI: 10.1126/science.aav4450. eprint: https://science.sciencemag.org/content/363/6428/eaav4450.full.pdf. URL: https://science.sciencemag.org/content/363/6428/eaav4450.

[21] Hans Luth. *Solid Surfaces, Interfaces and Thin Films*. Springer International Publishing, 2015. DOI: 10.1007/978-3-319-10756-1. URL: https://doi.org/10.1007%2F978-3-319-10756-1.

[22] Shuji Hasegawa. “Reflection High-Energy Electron Diffraction”. In: *Characterization of Materials*. American Cancer Society, 2012, pp. 1–14. ISBN: 9780471266969. DOI: 10.1002/0471266965.com139. eprint: https://onlinelibrary.wiley.com/doi/pdf/10.1002/0471266965.com139. URL: https://onlinelibrary.wiley.com/doi/abs/10.1002/0471266965.com139.

[23] Naoto Nagaosa et al. “Anomalous Hall effect”. In: *Rev. Mod. Phys.* 82 (2 May 2010), pp. 1539–1592. DOI: 10.1103/RevModPhys.82.1539. URL: https://link.aps.org/doi/10.1103/RevModPhys.82.1539.

[24] Katsuyuki Fukutani, Hiroshi Daimon, and Shozo Ino. “Reflection High-Energy Electron Diffraction Study of the Growth of Ge on the Ge(111) Surface”. In: *Japanese Journal of Applied Physics* 31.Part 1, No. 10 (Oct. 1992), pp. 3429–3435. DOI: 10.1143/jjap.31.3429. URL: https://doi.org/10.1143%2Fjjap.31.3429.

[25] Valeriy Yu. Verchenko et al. “Ferromagnetic Order, Strong Magnetocrystalline Anisotropy, and Magnetocaloric Effect in the Layered Telluride Fe3-δGeTe2”. In: *Inorganic Chemistry* 54.17 (2015). PMID: 26267350, pp. 8598–8607. DOI: 10.1021/acs.inorgchem.5b01260. eprint: https://doi.org/10.1021/acs.inorgchem.5b01260. URL: https://doi.org/10.1021/acs.inorgchem.5b01260.